



Numerical investigation of magnetic multiphase flows by the fractional-step-based multiphase lattice Boltzmann method

Cite as: Phys. Fluids **32**, 083309 (2020); <https://doi.org/10.1063/5.0020903>

Submitted: 07 July 2020 . Accepted: 28 July 2020 . Published Online: 17 August 2020

Xiang Li (李翔) , Zhi-Qiang Dong (董志强), Peng Yu (余鹏) , Xiao-Dong Niu (牛小东), Lian-Ping Wang (王连平), De-Cai Li (李德才), and Hiroshi Yamaguchi (山口博司)

COLLECTIONS

Paper published as part of the special topic on [Recent Advances in Theory, Simulations, and Experiments on Multiphase Flows](#)

Note: This paper is part of the Special Topic, Recent Advances in Theory, Simulations, and Experiments on Multiphase Flows.

 This paper was selected as an Editor's Pick



View Online



Export Citation



CrossMark

ARTICLES YOU MAY BE INTERESTED IN

[Retardation of droplet transport in confined microchannel by interfacial jamming of nanoparticles](#)

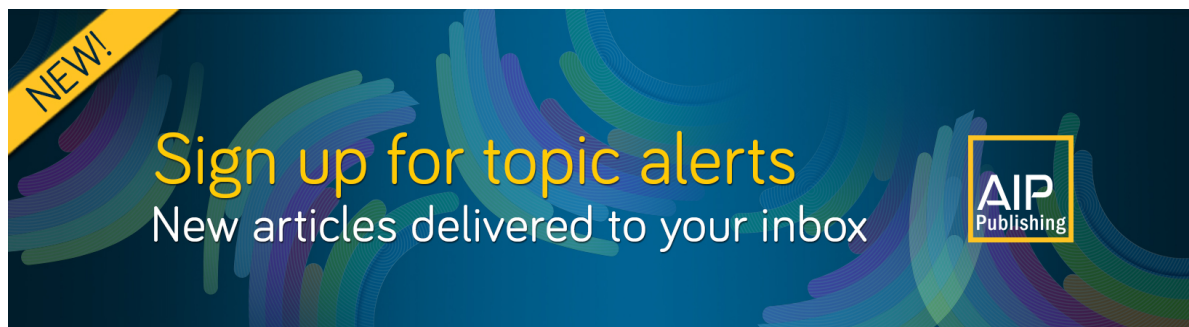
Physics of Fluids **32**, 087110 (2020); <https://doi.org/10.1063/5.0016450>

[Transport and fate of human expiratory droplets—A modeling approach](#)

Physics of Fluids **32**, 083307 (2020); <https://doi.org/10.1063/5.0021280>


[Effects of gravity and surface tension on steady microbubble propagation in asymmetric bifurcating airways](#)

Physics of Fluids **32**, 072105 (2020); <https://doi.org/10.1063/5.0012796>



NEW!

Sign up for topic alerts
New articles delivered to your inbox



Numerical investigation of magnetic multiphase flows by the fractional-step-based multiphase lattice Boltzmann method

Cite as: *Phys. Fluids* **32**, 083309 (2020); doi: [10.1063/5.0020903](https://doi.org/10.1063/5.0020903)

Submitted: 7 July 2020 • Accepted: 28 July 2020 •

Published Online: 17 August 2020





View Online



Export Citation



CrossMark

Xiang Li (李翔),^{1,2,3}  Zhi-Qiang Dong (董志强),^{1,2,3} Peng Yu (余鹏),^{2,3,4,5,a)}  Xiao-Dong Niu (牛小东),^{6,a)} Lian-Ping Wang (王连平),^{2,3,4,7} De-Cai Li (李德才),⁸ and Hiroshi Yamaguchi (山口博司)⁹

AFFILIATIONS

¹Harbin Institute of Technology, Harbin 515063, China

²Department of Mechanics and Aerospace Engineering, Southern University of Science and Technology, Shenzhen 518055, China

³Center for Complex Flows and Soft Matter Research, Southern University of Science and Technology, Shenzhen 518055, China

⁴Guangdong Provincial Key Laboratory of Turbulence Research and Applications, Southern University of Science and Technology, Shenzhen 518055, China

⁵Shenzhen Key Laboratory of Complex Aerospace Flows, Southern University of Science and Technology, Shenzhen 518055, China

⁶College of Engineering, Shantou University, 243 Daxue Road, Shantou 515063, China

⁷Department of Mechanical Engineering, University of Delaware, Newark, Delaware 19716-3140, USA

⁸Department of Mechanical Engineering, Tsinghua University, Beijing 100084, China

⁹Energy Conversion Research Center, Doshisha University, Kyoto 630-0321, Japan

Note: This paper is part of the Special Topic, Recent Advances in Theory, Simulations, and Experiments on Multiphase Flows.

^{a)} **Authors to whom correspondence should be addressed:** yup6@sustech.edu.cn and xdniu@stu.edu.cn

ABSTRACT

In the present study, a fractional-step-based multiphase lattice Boltzmann (LB) method coupled with a solution of a magnetic field evolution is developed to predict the interface behavior in magnetic multiphase flows. The incompressible Navier–Stokes equations are utilized for the flow field, while the Cahn–Hilliard equation is adopted to track the interface, and these governing equations are solved by reconstructing solutions within the LB framework with the prediction–correction step based on a fractional-step method. The proposed numerical model inherits the excellent performance of kinetic theory from the LB method and integrates the good numerical stability from the fractional-step method. Meanwhile, the macroscopic variables can be simply and directly calculated by the equilibrium distribution functions, which saves the virtual memories and simplifies the computational process. The proposed numerical model is validated by simulating two problems, i.e., a bubble rising with a density ratio of 1000 and a viscosity ratio of 100 and a stationary circular cylinder under an external uniform magnetic field. The interfacial deformations of a ferrofluid droplet in organic oil and an aqueous droplet in ferrofluid under the external magnetic field are, then, simulated, and the underlying mechanisms are discussed. Moreover, the rising process of a gas bubble in the ferrofluid is investigated, which shows that the rising velocity is accelerated under the effect of the external magnetic field. All the numerical examples demonstrate the capability of the present numerical method to handle the problem with the interfacial deformation in magnetic multiphase flows.

Published under license by AIP Publishing. <https://doi.org/10.1063/5.0020903>

I. INTRODUCTION

Magnetic fluids (ferrofluids) remain the flowability of fluids and the magnetizability of ferromagnets, in which a mass of magnetic nanoparticles are homogeneously dispersed into carrier

liquid (base fluid) by surface coating with a special surfactant. Ferrofluids were first invented by Bitter¹ in 1931 and then developed as a stable colloid by Elmore^{2,3} in 1938. The motions and interfacial behaviors of ferrofluid, such as Rosensweig instability,^{4,5} can be robustly controlled by applying an external magnetic field. These

good properties make the ferrofluids widely used in advanced medical science and industrial applications, such as magnetic hyperthermia,⁶ microfluidic manipulation,^{7–9} and heat transfer.^{10,11} To extend and improve those kinds of industrial application, the underlying mechanisms of magnetic multiphase flows need to be understood. After the pioneering works of Lord Rayleigh,¹² van der Waals,¹³ and Taylor,¹⁴ which built the fundamental theory of complex interfacial behaviors, various numerical descriptions have been proposed and developed in past decades, such as the volume of fluid (VOF) method, front tracking method, level set method, and diffuse interface method.¹⁵ The numerical model of multiphase flows based on the diffuse interface method can be divided into two categories: one is the direct numerical model based on the macroscopic Navier–Stokes equation, and the other is the lattice Boltzmann (LB) method based on the mesoscopic kinetic theory.^{16–18}

The LB method has attracted a great deal of interest from the academic community due to its unique properties, such as instinct kinetic nature, relatively low numerical dissipation, and simple algebraic calculation of the streaming-collision process. To adopt these features, various multiphase LB models have been developed to simulate multiphase flows, which can be categorized as the multiphase LB model, multiphase LB flux solver, and fractional-step-based multiphase LB model (the simplified multiphase LB method). The pioneering multiphase LB model, i.e., the Shan–Chen pseudopotential model, was proposed by Shan and Chen¹⁹ in 1992. Then, a free-energy LB model with double distribution functions (DDFs) was proposed to simulate the Rayleigh–Taylor instability.²⁰ Zheng *et al.*²¹ developed a multiphase LB model based on the DDF in which the Cahn–Hilliard (C–H) equation can be recovered by the LB equation, which can maintain the Galilean invariance property. The DDF strategy was developed and modified by various talented scientists and widely used to predict multi-physical field coupled flow and multi-component flow. Even significant development in the multiphase LB models has been achieved in past three decades, the inherent drawbacks, including the mass diffusion problem, the poor numerical stability at the large density ratio, the high computational redundancy, and the complicated implementation in the boundary condition of physical variables, become a limitation of this kind of numerical approach. To prevent the mass dissipation, Huang *et al.*²² developed a mass-conserving axisymmetric LB model. This kind of mass-correcting term is further performed in the LB flux solver²³ and the improved multiphase LB model.²⁴ The multiphase LB flux solver, incorporating the stability of the finite volume (FV) method and the kinetic nature of the LB method, was first proposed by Wang *et al.*²³ However, the fundamental drawbacks, i.e., the large memory consumption and the complex computational process, are introduced in the LB flux solver, even though a great improvement of numerical stability is achieved. To save the virtual memories and computational time during the numerical simulation, Yuan *et al.*²⁵ developed an LB flux solver by introducing an adaptive mesh refinement (AMR) algorithm. Another numerical approach proposed by Chen *et al.*²⁶ is called the simplified LB model. In that numerical model, the evolution of the density distribution function does not need to be solved, which can save the virtual memories efficiently.²⁶ Most recently, the simplified LB model was developed as an unconditionally stable LB model with truly second-order accuracy and extended to simulate the multiphase flows with the large density ratio.^{27–30}

Despite the fact that various successful multiphase LB models exist, there is still a challenging issue on simulating the magnetic multiphase flows with a large density ratio under an external magnetic field due to the complex interfacial behaviors and the magnetic interaction between the magnetic and non-magnetic materials. The LB model as a mesoscopic method has many unique properties mentioned above, but it is less used for the simulation of magnetic multiphase flows. To incorporate the external magnetic effect into the LB method, Niu *et al.*³¹ proposed an LB model with triple distribution functions for a single-phase heat transfer in the ferrofluid. In that model,³¹ the interaction between the magnetic and non-magnetic materials is ignored, and the magnetic effect relied on the temperature distribution function. Zhang and Che³² investigated the natural convection of magnetic fluid in an inclined cavity by using a multiple-relaxation-time thermal LB model with a constant magnetic force. The similar multiple-relaxation-time LB model with D3Q19 and D3Q17 models was developed by Sajjadi *et al.*,³³ and the magnetohydrodynamic natural convection in a three-dimensional cubic cavity is investigated. The representative limitation in the above-mentioned LB model is that the external magnetic force is set as a fixed value or related with the temperature distribution function, and thus, the evolution of the magnetic field and the calculation for the magnetic interaction are not involved. Moreover, the precise implementation of the magnetic effect plagued the academic community in the numerical simulation of magnetic fluid for many years. To approach this problem, Shi *et al.*³⁴ transferred the magnetic body force into a magneto-strictive force term by using the linearly elastic mechanics. After that, Ghaderi *et al.*³⁵ numerically investigated a falling ferrofluid droplet by using the Shan–Chen LB model with the magneto-strictive force term. Compared with the fixed magnetic force model, the computational process of the magneto-strictive force is related with the evolution of the external magnetic field, and the local change in the magnetic force is considered. However, the apparent drawback of the magneto-strictive force model is that the linearly elastic mechanics is used to approximate the magnetic force, which is hard to physically describe the effect of the external magnetic field. Hu *et al.*³⁶ developed a multiple-relaxation-time (MRT) LB model with triple distribution functions to simulate the ferrofluid droplet behaviors. The evolution of the external magnetic field is calculated by the MRT-LB model, but the computational process is rather complicated. Although the bubble merging process in the ferrofluid with a large density ratio was simulated by Hu *et al.*,³⁶ the equilibrium shape of the merged bubble was not consistent with the experimental results. Moreover, the magnetic flux interaction between the magnetic and non-magnetic materials is not involved in those numerical models.

To predict the interfacial behaviors of magnetic multiphase flows with high fidelity, it is necessary to develop an LB model, which has a clear numerical framework and a better numerical stability. Therefore, the purpose of this work is to develop a magnetic field coupling fractional-step-based LB method, which inherits the excellent performance of kinetic theory and the good numerical stability of the fractional-step method,³⁷ to simulate the dynamics and the interfacial behaviors of magnetic multiphase flow under an external uniform magnetic field. This numerical model is developed within the LB framework. The relation between macroscopic governing equations and the DDF in the LB model is established by the Chapman–Enskog expansion analysis, and then,

a prediction–correction strategy for the macroscopic physical variables by the fractional-step method³⁷ is reconstructed. To evaluate the external magnetic field with the interaction of magnetic flux density between the magnetic and non-magnetic regions, the Poisson equation solver with a self-correcting procedure³⁸ is employed. The Gaussian transformation is performed to transfer the magnetic body force to the magnetic surface force mathematically so that the effect of the external magnetic force can be directly incorporated into the external force term of the fractional-step-based LB equation.

The remainder of this article is organized as follows. In Sec. II, the macroscopic governing equations and the multiphase LB model with the DDF for magnetic multiphase flow are first introduced; the relation between mesoscopic variables and macroscopic variables is, then, established through the Chapman–Enskog expansion analysis; a multiphase LB model based on the fractional-step method is further presented; and the Poisson equation solver with a self-correcting procedure for solving the magnetic field is finally represented. In Sec. III, several typical physical problems, such as a bubble rising with a large density ratio, a stationary cylinder under an external uniform magnetic field, the magnetic induced interfacial deformation of a single ferrofluid droplet, the interfacial deformation of an aqueous droplet in the ferrofluid, and a bubble rising in the ferrofluid under an external magnetic field, are simulated to demonstrate the accuracy and capability of the present magnetic field coupling fractional-step-based multiphase lattice Boltzmann model. Finally, the conclusions are drawn in Sec. IV.

II. METHODOLOGY

A. Macroscopic governing equations

In this work, a fractional-step-based LB method is extended to simulate magnetic multiphase flows comprising of magnetic fluid and non-magnetic fluid. The governing equations for the incompressible, isothermal, and immiscible two-component flow with the magnetic effect include the continuity, momentum, and interface capturing equations, which read

$$\frac{\partial \rho}{\partial t} + \rho \nabla \cdot \mathbf{u} = 0, \quad (1)$$

$$\frac{\partial \rho \mathbf{u}}{\partial t} + \nabla \cdot (\rho \mathbf{u} \mathbf{u}) = -\nabla p + \nabla \left[\mu \cdot (\nabla \mathbf{u} + (\nabla \mathbf{u})^T) \right] + \mathbf{F}_g + \mathbf{F}_s + \mathbf{F}_m, \quad (2)$$

$$\frac{\partial C}{\partial t} + (\mathbf{u} \cdot \nabla) C = M \nabla^2 \mu_C, \quad (3)$$

where ρ , \mathbf{u} , p , and μ are the fluid density, velocity, pressure, and dynamic viscosity, respectively. M denotes the mobility of the C–H equation. The external forces include the gravitational force \mathbf{F}_g , the surface tension force \mathbf{F}_s , and the magnetic surface force \mathbf{F}_m , which can be expressed as

$$\mathbf{F}_g = \rho \mathbf{g}, \quad (4)$$

$$\mathbf{F}_s = -C \nabla \mu_C, \quad (5)$$

$$\mathbf{F}_m = \nabla \cdot \boldsymbol{\tau}_m, \quad (6)$$

where \mathbf{g} is the gravity, μ_C is the chemical potential, C is the order parameter varying in the range of $[0, 1]$, and $\boldsymbol{\tau}_m$ represents the magnetic stress tensor. The chemical potential can be written as³⁹

$$\mu_C = 2AC(C-1)(2C-1) - \kappa \nabla^2 C, \quad (7)$$

where A and κ are two constant parameters related with the interfacial thickness⁴⁰ W and the surface tension coefficient σ , which are given by

$$A = \frac{12\sigma}{W}, \quad (8)$$

$$\kappa = \frac{3W\sigma}{2}. \quad (9)$$

B. Multiphase lattice Boltzmann model

Under the multiphase lattice Boltzmann framework, the evolutions of the flow field and the interface are achieved by updating the distribution functions of the hydrodynamic field and the order parameter field, respectively. The lattice Boltzmann equations with DDFs for the N–S equations and the C–H equation are developed as

$$f_\alpha(\mathbf{r} + \mathbf{e}_\alpha \delta t, t + \delta t) - f_\alpha(\mathbf{r}, t) = -\frac{1}{\tau_f} (f_\alpha(\mathbf{r}, t) - f_\alpha^{eq}(\mathbf{r}, t)) + \mathbf{S}_\alpha \delta t, \quad (10)$$

$$g_\alpha(\mathbf{r} + \mathbf{e}_\alpha \delta t, t + \delta t) - g_\alpha(\mathbf{r}, t) = -\frac{1}{\tau_g} (g_\alpha(\mathbf{r}, t) - g_\alpha^{eq}(\mathbf{r}, t)), \quad (11)$$

with

$$\mathbf{S}_\alpha = \left(1 - \frac{1}{2\tau_f} \right) (\mathbf{e}_\alpha - \mathbf{u}) \cdot \{ \Gamma_\alpha(\mathbf{u}) (\mathbf{F}_g + \mathbf{F}_s + \mathbf{F}_m) - [\Gamma_\alpha(\mathbf{u}) - \Gamma_\alpha(0)] \nabla \zeta(\rho) \}, \quad (12)$$

$$\Gamma_\alpha(\mathbf{u}) = \omega_\alpha \left[1 + \frac{\mathbf{e}_\alpha \cdot \mathbf{u}}{c_s^2} + \frac{(\mathbf{e}_\alpha \cdot \mathbf{u})^2}{2c_s^4} - \frac{|\mathbf{u}|^2}{2c_s^2} \right], \quad (13)$$

$$\zeta(\rho) = p - \rho RT = p - \rho c_s^2, \quad (14)$$

$$\begin{aligned} f_\alpha^{eq}(\mathbf{r}, t) &= \rho c_s^2 \Gamma_\alpha(\mathbf{u}) + \zeta(\rho) \Gamma_\alpha(0) \\ &= \omega_\alpha \left[p + \rho c_s^2 \left(\frac{\mathbf{e}_\alpha \cdot \mathbf{u}}{c_s^2} + \frac{(\mathbf{e}_\alpha \cdot \mathbf{u})^2}{2c_s^4} - \frac{|\mathbf{u}|^2}{2c_s^2} \right) \right], \end{aligned} \quad (15)$$

$$g_\alpha^{eq} = \begin{cases} C - \mu_C Q (1 - \omega_0) / c_s^2, & \alpha = 0, \\ \omega_\alpha (\mu_C Q + C \mathbf{e}_\alpha \cdot \mathbf{u}) / c_s^2, & \alpha = 1 - 8, \end{cases} \quad (16)$$

where $f_\alpha(\mathbf{r}, t)$ and $g_\alpha(\mathbf{r}, t)$ are the distribution functions of the hydrodynamic field and the order parameter field with the lattice velocity \mathbf{e}_α and the weighting coefficient ω_α , respectively; $f_\alpha^{eq}(\mathbf{r}, t)$ and $g_\alpha^{eq}(\mathbf{r}, t)$ are the corresponding equilibrium distribution functions of the hydrodynamic field and the order parameter field, respectively; δt represents the time interval; \mathbf{S}_α denotes the external force term, in which \mathbf{F}_g , \mathbf{F}_s , and \mathbf{F}_m are the gravitational force, surface tension force, and magnetic surface force in Eq. (2); $\zeta(\rho)$ is the incompressible transformation term, which is related with the pressure,²⁰ τ_f and

τ_g are the single relaxation parameters in the LB equation for the N–S equations and the C–H equation, respectively, which are related to the dynamic viscosity μ and the diffusion parameter Q through

$$\tau_f = \frac{\mu}{\rho c_s^2 \delta t} + \frac{1}{2}, \quad (17)$$

$$\tau_g = \frac{M}{Q \delta t} + \frac{1}{2}, \quad (18)$$

where c_s is the speed of sound and Q is the diffusion parameter. The D2Q9 lattice model⁴¹ is adopted in the present work, and the corresponding lattice velocity and weighting coefficients are given as

$$\mathbf{e}_\alpha = \begin{cases} (0, 0), & \alpha = 0, \\ c \left[\cos\left(\frac{(\alpha-1)\pi}{2}\right), \sin\left(\frac{(\alpha-1)\pi}{2}\right) \right], & \alpha = 1, 2, 3, 4, \\ \sqrt{2}c \left[\cos\left(\frac{(\alpha-1)\pi}{2}\right), \sin\left(\frac{(\alpha-1)\pi}{2}\right) \right], & \alpha = 5, 6, 7, 8, \end{cases} \quad (19)$$

$$\begin{aligned} \omega_\alpha &= [\omega_0 \ \omega_1 \ \omega_2 \ \omega_3 \ \omega_4 \ \omega_5 \ \omega_6 \ \omega_7 \ \omega_8]^T \\ &= \left[\frac{4}{9} \ \frac{1}{9} \ \frac{1}{9} \ \frac{1}{9} \ \frac{1}{9} \ \frac{1}{36} \ \frac{1}{36} \ \frac{1}{36} \ \frac{1}{36} \right]^T, \end{aligned} \quad (20)$$

where $c = \delta r / \delta t$ is set as 1 and δr represents the lattice spacing.

C. Chapman–Enskog expansion analysis

The LB framework is established in the mesoscopic scale based on the kinetic theory. To derive the fractional-step-based multiphase LB model, the macroscopic variables recovered from the original LB model need to be obtained first. The Chapman–Enskog expansion analysis,⁴² as one of the multiscale analysis, is always performed to construct the relation between the mesoscopic scale and the macroscopic scale. In this part, the macroscopic governing equations, i.e., the N–S equations and the C–H equation, are recovered from the multiphase LB model through the Chapman–Enskog expansion analysis. The distribution functions, the space and time derivatives, and the force term can be defined in multiscale as follows:

$$f_\alpha = f_\alpha^{(0)} + \varepsilon f_\alpha^{(1)} + \varepsilon^2 f_\alpha^{(2)}, \quad g_\alpha = g_\alpha^{(0)} + \varepsilon g_\alpha^{(1)} + \varepsilon^2 g_\alpha^{(2)}, \quad (21)$$

$$\frac{\partial}{\partial t} = \varepsilon \frac{\partial}{\partial t_0} + \varepsilon^2 \frac{\partial}{\partial t_1}, \quad \nabla = \varepsilon \nabla_1, \quad (22)$$

$$S_\alpha = \varepsilon S_\alpha^{(1)}, \quad (23)$$

where ε is a small expansion parameter. Substituting Eqs. (21)–(23) into Eqs. (10) and (11) yields

$$\begin{aligned} & \left(\varepsilon \frac{\partial}{\partial t_0} + \varepsilon^2 \frac{\partial}{\partial t_1} + \varepsilon \mathbf{e}_\alpha \cdot \nabla_1 \right) \left[f_\alpha^{(0)} + \varepsilon f_\alpha^{(1)} + \varepsilon^2 f_\alpha^{(2)} \right] \\ & + \frac{\delta t}{2} \left(\varepsilon \frac{\partial}{\partial t_0} + \varepsilon^2 \frac{\partial}{\partial t_1} + \varepsilon \mathbf{e}_\alpha \cdot \nabla_1 \right)^2 \left[f_\alpha^{(0)} + \varepsilon f_\alpha^{(1)} + \varepsilon^2 f_\alpha^{(2)} \right] + O(\delta t^2) \\ & = -\frac{1}{\tau_f \delta t} \left[f_\alpha^{(0)} + \varepsilon f_\alpha^{(1)} + \varepsilon^2 f_\alpha^{(2)} - f_\alpha^{eq} \right] + \varepsilon S_\alpha^{(1)}, \end{aligned} \quad (24)$$

$$\begin{aligned} & \left(\varepsilon \frac{\partial}{\partial t_0} + \varepsilon^2 \frac{\partial}{\partial t_1} + \varepsilon \mathbf{e}_\alpha \cdot \nabla_1 \right) \left[g_\alpha^{(0)} + \varepsilon g_\alpha^{(1)} + \varepsilon^2 g_\alpha^{(2)} \right] \\ & + \frac{\delta t}{2} \left(\varepsilon \frac{\partial}{\partial t_0} + \varepsilon^2 \frac{\partial}{\partial t_1} + \varepsilon \mathbf{e}_\alpha \cdot \nabla_1 \right)^2 \left[g_\alpha^{(0)} + \varepsilon g_\alpha^{(1)} + \varepsilon^2 g_\alpha^{(2)} \right] \\ & = -\frac{1}{\tau_g \delta t} \left[g_\alpha^{(0)} + \varepsilon g_\alpha^{(1)} + \varepsilon^2 g_\alpha^{(2)} - g_\alpha^{eq} \right]. \end{aligned} \quad (25)$$

From Eqs. (24) and (25), the following relations in different scales can be given as

$$\varepsilon^0 : f_\alpha^{(0)} = f_\alpha^{eq}, \quad (26a)$$

$$\varepsilon^0 : g_\alpha^{(0)} = g_\alpha^{eq}, \quad (26b)$$

$$\varepsilon^1 : \left(\frac{\partial}{\partial t_0} + \mathbf{e}_\alpha \cdot \nabla_1 \right) f_\alpha^{(0)} = -\frac{1}{\tau_f \delta t} f_\alpha^{(1)} + S_\alpha^{(1)}, \quad (27a)$$

$$\varepsilon^1 : \left(\frac{\partial}{\partial t_0} + \mathbf{e}_\alpha \cdot \nabla_1 \right) g_\alpha^{(0)} = -\frac{1}{\tau_g \delta t} g_\alpha^{(1)}, \quad (27b)$$

$$\begin{aligned} \varepsilon^2 : & \frac{\partial}{\partial t_1} f_\alpha^{(0)} + \left(1 - \frac{1}{2\tau_f} \right) \left(\frac{\partial}{\partial t_0} + \mathbf{e}_\alpha \cdot \nabla_1 \right) f_\alpha^{(1)} \\ & = -\frac{1}{\tau_f \delta t} f_\alpha^{(2)} - \frac{\delta t}{2} \left(\frac{\partial}{\partial t_0} + \mathbf{e}_\alpha \cdot \nabla_1 \right) S_\alpha^{(1)}, \end{aligned} \quad (28a)$$

$$\varepsilon^2 : \frac{\partial}{\partial t_1} g_\alpha^{(0)} + \left(1 - \frac{1}{2\tau_g} \right) \left(\frac{\partial}{\partial t_0} + \mathbf{e}_\alpha \cdot \nabla_1 \right) g_\alpha^{(1)} = -\frac{1}{\tau_g \delta t} g_\alpha^{(2)}. \quad (28b)$$

Then, the relations between the mesoscopic component and the macroscopic component are established, which read

$$\sum_\alpha f_\alpha^{eq} = p, \quad \sum_\alpha \mathbf{e}_\alpha f_\alpha^{eq} = \rho \mathbf{u} c_s^2, \quad \sum_\alpha \mathbf{e}_\alpha \mathbf{e}_\beta f_\alpha^{eq} = \rho \mathbf{u} \mathbf{u} c_s^2 + p c_s^2, \quad (29a)$$

$$\sum_\alpha g_\alpha^{eq} = C, \quad \sum_\alpha \mathbf{e}_\alpha g_\alpha^{eq} = \mathbf{C} \mathbf{u}, \quad \sum_\alpha \mathbf{e}_\alpha \mathbf{e}_\alpha g_\alpha^{eq} = \mathbf{C} \mathbf{u} \mathbf{u} + Q \mu_C c_s^2, \quad (29b)$$

$$\begin{aligned} \sum_\alpha f_\alpha^{(1)} &= -\frac{\delta t}{2} \mathbf{u} \cdot \nabla_1 \rho c_s^2, \quad \sum_\alpha \mathbf{e}_\alpha f_\alpha^{(1)} \\ &= -\frac{\delta t}{2} c_s^2 (\mathbf{F}_g + \mathbf{F}_s + \mathbf{F}_m), \quad \sum_\alpha f_\alpha^{(2)} = 0, \end{aligned} \quad (30a)$$

$$\begin{aligned} \sum_\alpha g_\alpha^{(1)} &= 0, \quad \sum_\alpha \mathbf{e}_\alpha g_\alpha^{(1)} = -\tau_g \delta t \left[\frac{\partial}{\partial t_0} (\mathbf{C} \mathbf{u}) + \nabla \cdot (\mathbf{C} \mathbf{u} \mathbf{u} + c_s^2 Q \mu_C) \right], \quad \sum_\alpha g_\alpha^{(2)} = 0, \end{aligned} \quad (30b)$$

$$\begin{aligned} \sum_\alpha S_\alpha^{(1)} &= \left(1 - \frac{1}{2\tau_f} \right) \mathbf{u} \cdot \nabla_1 \rho c_s^2, \quad \sum_\alpha \mathbf{e}_\alpha S_\alpha^{(1)} \\ &= \left(1 - \frac{1}{2\tau_f} \right) c_s^2 (\mathbf{F}_g + \mathbf{F}_s + \mathbf{F}_m). \end{aligned} \quad (30c)$$

The nonequilibrium parts in Eqs. (27a) and (27b) are represented as

$$f_{\alpha}^{neq} = f_{\alpha} - f_{\alpha}^{eq} \sim \epsilon f_{\alpha}^{(1)} = -\tau_f \delta t \left[\left(\frac{\partial}{\partial t} + \mathbf{e}_{\alpha} \cdot \nabla \right) f_{\alpha}^{eq} - S_{\alpha} \right], \quad (31a)$$

$$g_{\alpha}^{neq} = g_{\alpha} - g_{\alpha}^{eq} \sim \epsilon g_{\alpha}^{(1)} = -\tau_g \delta t \left(\frac{\partial}{\partial t} + \mathbf{e}_{\alpha} \cdot \nabla \right) g_{\alpha}^{eq}, \quad (31b)$$

$$\sum_{\alpha} f_{\alpha}^{neq} = -\frac{\delta t}{2} c_s^2 \mathbf{u} \cdot \nabla \rho, \quad \sum_{\alpha} \mathbf{e}_{\alpha} f_{\alpha}^{neq} = -\frac{\delta t}{2} c_s^2 (\mathbf{F}_g + \mathbf{F}_s + \mathbf{F}_m), \quad (32)$$

$$\sum_{\alpha} g_{\alpha}^{neq} = 0.$$

The equivalent macroscopic governing equations can be recovered by assembling the zeroth and first order moments of Eqs. (27) and (28), which can be written as

$$\frac{\partial p}{\partial t} + \nabla \cdot \sum_{\alpha} \mathbf{e}_{\alpha} f_{\alpha}^{eq} = \mathbf{u} \cdot \nabla \rho c_s^2, \quad (33)$$

$$\frac{\partial \rho \mathbf{u} c_s^2}{\partial t} + \nabla \cdot \sum_{\alpha} \mathbf{e}_{\alpha} \mathbf{e}_{\alpha} \left[f_{\alpha}^{eq} + \left(1 - \frac{1}{2\tau_f} \right) f_{\alpha}^{neq} \right] + \frac{\delta t}{2} \nabla \cdot \sum_{\alpha} \mathbf{e}_{\alpha} \mathbf{e}_{\alpha} S_{\alpha} = c_s^2 (\mathbf{F}_g + \mathbf{F}_s + \mathbf{F}_m), \quad (34)$$

$$\frac{\partial C}{\partial t} + \nabla \cdot \sum_{\alpha} \mathbf{e}_{\alpha} g_{\alpha}^{eq} + \left(1 - \frac{1}{2\tau_g} \right) \nabla \cdot \sum_{\alpha} \mathbf{e}_{\alpha} g_{\alpha}^{neq} = 0. \quad (35)$$

D. Fractional-step-based multiphase lattice Boltzmann model

The substance of the fractional-step-based LB model is to reconstruct the relations between the mesoscopic variables and the macroscopic variables through the Chapman–Enskog expansion analysis. The macroscopic variables are solved by using a prediction–correction strategy, which is based on the fractional-step method.^{26,30,35} Following the similar mathematical procedure of the simplified multiphase LB method by Chen *et al.*,^{26,30} Eqs. (33)–(35) are separated into two parts, i.e., the prediction part and the correction part.

In the prediction step, the reconstructing macroscopic governing equations separated from Eqs. (33)–(35) can be written as follows:

$$\frac{\partial p}{\partial t} + \nabla \cdot \sum_{\alpha} \mathbf{e}_{\alpha} f_{\alpha}^{eq} - \mathbf{u} \cdot \nabla \rho c_s^2 = 0, \quad (36a)$$

$$\frac{\partial \rho \mathbf{u} c_s^2}{\partial t} + \nabla \cdot \sum_{\alpha} \mathbf{e}_{\alpha} \mathbf{e}_{\alpha} \left[f_{\alpha}^{eq} - \frac{\delta t}{2} \left(\frac{\partial}{\partial t} + \mathbf{e}_{\alpha} \cdot \nabla \right) f_{\alpha}^{eq} \right] = 0, \quad (36b)$$

$$\frac{\partial C}{\partial t} + \nabla \cdot \left[\sum_{\alpha} \mathbf{e}_{\alpha} g_{\alpha}^{eq} - \frac{\delta t}{2} \sum_{\alpha} \mathbf{e}_{\alpha} \left(\frac{\partial}{\partial t} + \mathbf{e}_{\alpha} \cdot \nabla \right) g_{\alpha}^{eq} \right] = 0. \quad (36c)$$

The intermediate hydrodynamic variables and the intermediate order parameter are given as

$$\tilde{p} = \sum_{\alpha} f_{\alpha}^{eq-c}(\mathbf{r} - \mathbf{e}_{\alpha} \delta t, t - \delta t), \quad (37a)$$

$$\tilde{\rho} \tilde{\mathbf{u}} c_s^2 = \sum_{\alpha} \mathbf{e}_{\alpha} f_{\alpha}^{eq}(\mathbf{r} - \mathbf{e}_{\alpha} \delta t, t - \delta t), \quad (37b)$$

$$\tilde{C} = \sum_{\alpha} g_{\alpha}^{eq}(\mathbf{r} - \mathbf{e}_{\alpha} \delta t, t - \delta t), \quad (37c)$$

where the superscript “*eq-c*” denotes the equilibrium distribution function calculated by the density on the central mesh node and the hydrodynamic variables on the streaming nodes. By adopting the Taylor series expansion analysis, the above equilibrium distribution function can be written as

$$f_{\alpha}^{eq-c}(\mathbf{r} - \mathbf{e}_{\alpha} \delta t, t - \delta t) = f_{\alpha}^{eq}(\mathbf{r} - \mathbf{e}_{\alpha} \delta t, t - \delta t) + [\Gamma_{\alpha}(\mathbf{u}) - \Gamma_{\alpha}(0)] \mathbf{e}_{\alpha} \delta t \cdot \nabla \rho c_s^2 + O(\delta t^2), \quad (38a)$$

$$f_{\alpha}^{eq}(\mathbf{r} - \mathbf{e}_{\alpha} \delta t, t - \delta t) = f_{\alpha}^{eq}(\mathbf{r}, t) - \delta t \left(\frac{\partial}{\partial t} + \mathbf{e}_{\alpha} \cdot \nabla \right) f_{\alpha}^{eq}(\mathbf{r}, t) + \frac{\delta t^2}{2} \left(\frac{\partial}{\partial t} + \mathbf{e}_{\alpha} \cdot \nabla \right)^2 f_{\alpha}^{eq}(\mathbf{r}, t) + O(\delta t^3), \quad (38b)$$

$$g_{\alpha}^{eq}(\mathbf{r} - \mathbf{e}_{\alpha} \delta t, t - \delta t) = g_{\alpha}^{eq}(\mathbf{r}, t) - \delta t \left(\frac{\partial}{\partial t} + \mathbf{e}_{\alpha} \cdot \nabla \right) g_{\alpha}^{eq}(\mathbf{r}, t) + \frac{\delta t^2}{2} \left(\frac{\partial}{\partial t} + \mathbf{e}_{\alpha} \cdot \nabla \right)^2 g_{\alpha}^{eq}(\mathbf{r}, t) + O(\delta t^3). \quad (38c)$$

Substituting Eqs. (38a)–(38c) into Eqs. (37a)–(37c) and applying the similar mathematical procedure of Chen *et al.*,³⁰ the reconstructing macroscopic governing equations can be recovered as

$$\tilde{p} = \sum_{\alpha} f_{\alpha}^{eq-c}(\mathbf{r} - \mathbf{e}_{\alpha} \delta t, t - \delta t) = p - \delta t \left[\frac{\partial p}{\partial t} + \nabla \cdot \sum_{\alpha} \mathbf{e}_{\alpha} f_{\alpha}^{eq} - \mathbf{u} \cdot \nabla \rho c_s^2 + O(\delta t) \right], \quad (39a)$$

$$\tilde{\rho} \tilde{\mathbf{u}} c_s^2 = \sum_{\alpha} \mathbf{e}_{\alpha} f_{\alpha}^{eq}(\mathbf{r} - \mathbf{e}_{\alpha} \delta t, t - \delta t) = \rho \mathbf{u} c_s^2 - \delta t \left\{ \frac{\partial \rho \mathbf{u} c_s^2}{\partial t} + \nabla \cdot \sum_{\alpha} \mathbf{e}_{\alpha} \mathbf{e}_{\alpha} \left[f_{\alpha}^{eq} - \frac{\delta t}{2} \left(\frac{\partial}{\partial t} + \mathbf{e}_{\alpha} \cdot \nabla \right) f_{\alpha}^{eq} \right] + O(\delta t^2) \right\}, \quad (39b)$$

$$\tilde{C} = \sum_{\alpha} g_{\alpha}^{eq}(\mathbf{r} - \mathbf{e}_{\alpha} \delta t, t - \delta t) = C - \delta t \left\{ \frac{\partial C}{\partial t} + \nabla \cdot \left[\sum_{\alpha} \mathbf{e}_{\alpha} g_{\alpha}^{eq} - \frac{\delta t}{2} \sum_{\alpha} \mathbf{e}_{\alpha} \left(\frac{\partial}{\partial t} + \mathbf{e}_{\alpha} \cdot \nabla \right) g_{\alpha}^{eq} \right] + O(\delta t^2) \right\}. \quad (39c)$$

In the correction step, the reconstructing macroscopic governing equations can be written as follows:

$$\frac{\partial p}{\partial t} = 0, \quad (40a)$$

$$\frac{\partial \rho \mathbf{u} c_s^2}{\partial t} - \nabla \cdot (\tau_f - 1) \sum_{\alpha} \mathbf{e}_{\alpha} \mathbf{e}_{\alpha} \delta t \left(\frac{\partial}{\partial t} + \mathbf{e}_{\alpha} \cdot \nabla \right) f_{\alpha}^{eq} + \nabla \cdot \tau_f \delta t \sum_{\alpha} \mathbf{e}_{\alpha} \mathbf{e}_{\alpha} S_{\alpha} = c_s^2 (\mathbf{F}_g + \mathbf{F}_s + \mathbf{F}_m), \quad (40b)$$

$$\frac{\partial C}{\partial t} - \nabla \cdot (\tau_g - 1) \delta t \sum_{\alpha} \mathbf{e}_{\alpha} \left(\frac{\partial}{\partial t} + \mathbf{e}_{\alpha} \cdot \nabla \right) g_{\alpha}^{eq} = 0. \quad (40c)$$

The hydrodynamics variables and the order parameter are given as

$$p = \tilde{p}, \quad (41a)$$

$$\begin{aligned} \rho \mathbf{u} c_s^2 = & \tilde{\rho} \tilde{\mathbf{u}} c_s^2 + \sum_{\alpha} \mathbf{e}_{\alpha} \left[\tilde{f}_{\alpha}^{eq} \left(\mathbf{r} + \frac{\delta t}{2} \mathbf{e}_{\alpha}, t - \frac{\delta t}{2} \right) - \tilde{f}_{\alpha}^{eq} \left(\mathbf{r} - \frac{\delta t}{2} \mathbf{e}_{\alpha}, t - \frac{\delta t}{2} \right) \right] \\ & - \frac{\delta t}{2} \sum_{\alpha} \mathbf{e}_{\alpha} \left[\tilde{S}_{\alpha} \left(\mathbf{r} + \frac{\delta t}{2} \mathbf{e}_{\alpha}, t - \frac{\delta t}{2} \right) - \tilde{S}_{\alpha} \left(\mathbf{r} - \frac{\delta t}{2} \mathbf{e}_{\alpha}, t - \frac{\delta t}{2} \right) \right] \\ & + c_s^2 (\mathbf{F}_g + \mathbf{F}_s + \mathbf{F}_m) \delta t, \end{aligned} \quad (41b)$$

$$C = \tilde{C} + \sum_{\alpha} \mathbf{e}_{\alpha} \left[\tilde{g}_{\alpha}^{eq} \left(\mathbf{r} + \frac{\delta t}{2} \mathbf{e}_{\alpha}, t - \frac{\delta t}{2} \right) - \tilde{g}_{\alpha}^{eq} \left(\mathbf{r} - \frac{\delta t}{2} \mathbf{e}_{\alpha}, t - \frac{\delta t}{2} \right) \right], \quad (41c)$$

with

$$\tilde{f}_{\alpha}^{eq} \left(\mathbf{r} + \frac{\delta t}{2} \mathbf{e}_{\alpha}, t - \frac{\delta t}{2} \right) = \left[\tau_f \left(\mathbf{r} + \frac{\delta t}{2} \mathbf{e}_{\alpha}, t - \frac{\delta t}{2} \right) - 1 \right] \left[f_{\alpha}^{eq}(\mathbf{r} + \mathbf{e}_{\alpha} \delta t, t) - f_{\alpha}^{eq}(\mathbf{r}, t - \delta t) \right], \quad (42a)$$

$$\tilde{f}_{\alpha}^{eq} \left(\mathbf{r} - \frac{\delta t}{2} \mathbf{e}_{\alpha}, t - \frac{\delta t}{2} \right) = \left[\tau_f \left(\mathbf{r} - \frac{\delta t}{2} \mathbf{e}_{\alpha}, t - \frac{\delta t}{2} \right) - 1 \right] \left[f_{\alpha}^{eq}(\mathbf{r}, t) - f_{\alpha}^{eq}(\mathbf{r} - \mathbf{e}_{\alpha} \delta t, t - \delta t) \right], \quad (42b)$$

$$\tilde{S}_{\alpha} = \tau_f S_{\alpha}, \quad (42c)$$

$$\tilde{g}_{\alpha}^{eq} \left(\mathbf{r} + \frac{\delta t}{2} \mathbf{e}_{\alpha}, t - \frac{\delta t}{2} \right) = g_{\alpha}^{eq}(\mathbf{r} + \mathbf{e}_{\alpha} \delta t, t) - g_{\alpha}^{eq}(\mathbf{r}, t - \delta t), \quad (42d)$$

$$\tilde{g}_{\alpha}^{eq} \left(\mathbf{r} - \frac{\delta t}{2} \mathbf{e}_{\alpha}, t - \frac{\delta t}{2} \right) = g_{\alpha}^{eq}(\mathbf{r}, t) - g_{\alpha}^{eq}(\mathbf{r} - \mathbf{e}_{\alpha} \delta t, t - \delta t). \quad (42e)$$

Similar to the recovering process in the prediction step, the reconstructing macroscopic governing equation in the correction step can be recovered from Eq. (41) by using the Taylor series expansion analysis. The above equilibrium distribution function can be written as

$$\begin{aligned} \tilde{f}_{\alpha}^{eq} \left(\mathbf{r} \pm \frac{\delta t}{2} \mathbf{e}_{\alpha}, t - \frac{\delta t}{2} \right) = & \delta t \left[\tau_f \left(\mathbf{r}, t - \frac{\delta t}{2} \right) - 1 \right] \left(\frac{\partial}{\partial t} + \mathbf{e}_{\alpha} \cdot \nabla \right) f_{\alpha}^{eq} \\ & \cdot \left(\mathbf{r}, t - \frac{\delta t}{2} \right) \pm \frac{\delta t^2}{2} \mathbf{e}_{\alpha} \cdot \nabla \left[\tau_f \left(\mathbf{r}, t - \frac{\delta t}{2} \right) - 1 \right] \\ & \cdot \left(\frac{\partial}{\partial t} + \mathbf{e}_{\alpha} \cdot \nabla \right) f_{\alpha}^{eq} \left(\mathbf{r}, t - \frac{\delta t}{2} \right) + O(\delta t^3), \end{aligned} \quad (43a)$$

$$\begin{aligned} \tilde{S}_{\alpha} \left(\mathbf{r} \pm \mathbf{e}_{\alpha} \delta t, t - \frac{\delta t}{2} \right) = & \delta t \tau_f \left(\mathbf{r}, t - \frac{\delta t}{2} \right) S_{\alpha} \left(\mathbf{r}, t - \frac{\delta t}{2} \right) \\ & \pm \delta t^2 \mathbf{e}_{\alpha} \cdot \nabla \left[\tau_f \left(\mathbf{r}, t - \frac{\delta t}{2} \right) - 1 \right] S_{\alpha} \left(\mathbf{r}, t - \frac{\delta t}{2} \right) \\ & + O(\delta t^3), \end{aligned} \quad (43b)$$

$$\begin{aligned} \tilde{g}_{\alpha}^{eq} \left(\mathbf{r} \pm \frac{\delta t}{2} \mathbf{e}_{\alpha}, t - \frac{\delta t}{2} \right) = & \delta t \left(\frac{\partial}{\partial t} + \mathbf{e}_{\alpha} \cdot \nabla \right) g_{\alpha}^{eq} \left(\mathbf{r}, t - \frac{\delta t}{2} \right) \\ & \pm \frac{\delta t^2}{2} \mathbf{e}_{\alpha} \cdot \nabla \left(\frac{\partial}{\partial t} + \mathbf{e}_{\alpha} \cdot \nabla \right) g_{\alpha}^{eq} \left(\mathbf{r}, t - \frac{\delta t}{2} \right) \\ & + O(\delta t^3). \end{aligned} \quad (43c)$$

Substituting Eqs. (43a)–(43c) into Eqs. (41a)–(41c) gives

$$\frac{p - \tilde{p}}{\delta t} = 0, \quad (44a)$$

$$\begin{aligned} \frac{\rho \mathbf{u} c_s^2 - \tilde{\rho} \tilde{\mathbf{u}} c_s^2}{\delta t} = & \left[\nabla \cdot (\tau_f - 1) \sum_{\alpha} \mathbf{e}_{\alpha i} \mathbf{e}_{\alpha j} \delta t \left(\frac{\partial}{\partial t} + \mathbf{e}_{\alpha} \cdot \nabla \right) f_{\alpha}^{eq} \right. \\ & \left. - \nabla \cdot \tau_f \delta t \sum_{\alpha} \mathbf{e}_{\alpha i} \mathbf{e}_{\alpha m} S_{\alpha} + c_s^2 (\mathbf{F}_g + \mathbf{F}_s + \mathbf{F}_m) \right]_{\mathbf{r}, t - 0.5 \delta t} \\ & + O(\delta t^2), \end{aligned} \quad (44b)$$

$$\begin{aligned} \frac{C - \tilde{C}}{\delta t} = & \left[\nabla \cdot (\tau_g - 1) \delta t \sum_{\alpha} \mathbf{e}_{\alpha} \left(\frac{\partial}{\partial t} + \mathbf{e}_{\alpha} \cdot \nabla \right) g_{\alpha}^{eq} \right]_{\mathbf{r}, t - 0.5 \delta t} \\ & + O(\delta t^2). \end{aligned} \quad (44c)$$

From the Taylor series expansion analysis, except that the reconstructing continuity equation in the prediction step is in the first order accuracy, which is shown in Eq. (39a), the rest of the reconstructing macroscopic governing equations are in the second-order accuracy. However, the approximation of the reconstructing continuity equation is acceptable in the numerical simulations of incompressible, isothermal, and immiscible two-component flow due to the incompressible limit and its capability to predict a relatively smooth pressure field. Therefore, the proposed model inherits the excellent performances of the kinetic theory from the LB method and integrates the good numerical stability from the fractional-step method. Meanwhile, the macroscopic variables can be simply and directly calculated by the equilibrium distribution functions instead of solving the evolution of the density distribution function, which saves the virtual memories and simplifies the computational process.

E. Magnetic field and magnetic surface force

To precisely calculate the distribution of the magnetic field with the consideration of the magnetic flux density on the interface between the magnetic and non-magnetic regions, a Poisson equation solver with a self-correcting procedure for the evolution of the external magnetic field is first introduced. The magnetic body force can, then, be derived from the Lorentz force and the static Maxwell equations. To physically describe the magnetic effect, the magnetic dipole force (Kelvin magnetic force) for the non-conducting ferrofluid obtained from the magnetic body force is transformed into the magnetic surface force by a rigorous mathematical procedure developed by Rosensweig.⁴³

The static uniform magnetic field can be described by the following Maxwell equations:⁴³

$$\nabla \cdot \mathbf{B} = 0, \quad (45a)$$

$$\nabla \times \mathbf{H} = \mathbf{J}, \quad (45b)$$

where \mathbf{B} is the magnetic flux density, \mathbf{H} is the magnetic intensity, and \mathbf{J} is the electric current density. For the non-conducting ferrofluid, the electric current density approximates to zero, and the relation between \mathbf{B} and \mathbf{H} can be represented as

$$\mathbf{B} = \eta_0 (\mathbf{H} + \mathbf{M}) = \eta_0 (1 + \chi) \mathbf{H} = \eta \mathbf{H}, \quad (46)$$

where \mathbf{M} is the magnetization, η is the magnetic permeability, and χ is the relative magnetic susceptibility. The vacuum magnetic permeability η_0 is $4\pi \times 10^{-7}$ N/A². The magnetic intensity can be determined by the magnetic scalar potential ψ through

$$\mathbf{H} = -\nabla\psi. \tag{47}$$

Substituting Eqs. (46) and (47) into Gauss's law for magnetism [Eq. (45a)], the following magnetic potential equation can be obtained:

$$\nabla \cdot (\eta\nabla\psi) = 0. \tag{48}$$

To ensure the conservation law for the electric current density, a Poisson equation solver with a self-correcting procedure based on Ohm's law and the Maxwell equation is used to predict the distribution and evolution of the magnetic field, which can be written as^{38,44,45}

$$\nabla^2\psi^{i+1} = \frac{1}{\eta} \left(1 - \frac{1}{\varepsilon_B}\right) \nabla \cdot \mathbf{B}^i, \tag{49a}$$

$$\mathbf{B}^* = -\eta\nabla\psi^{i+1}, \tag{49b}$$

$$\mathbf{B}^{i+1} = \mathbf{B}^i + \varepsilon_B(\mathbf{B}^* - \mathbf{B}^i), \tag{49c}$$

where ε_B is the relation coefficient ($0 < \varepsilon_B < 1$) and \mathbf{B}^i , \mathbf{B}^* , and \mathbf{B}^{i+1} are the magnetic flux densities at the i iteration step, the intermediate step, and the $i + 1$ iteration step, respectively. In the present work, to satisfy the conservation law, the numerical calculation process continues until the self-correcting procedure term of Eq. (49b) becomes sufficiently small (lower than 10^{-5}). To solve the interaction between the magnetic and non-magnetic regions, the conjugate boundary condition is implemented. Based on the Lorentz force law, the resultant force \mathbf{f} of the magnet field \mathbf{B} and the electric field \mathbf{E} can be written as

$$d\mathbf{f} = q(\mathbf{E} + \mathbf{v} \times \mathbf{B}), \tag{50}$$

where q is the electric charge with the instantaneous velocity \mathbf{v} . Thus, the Lorentz body force per unit volume can be described as

$$\mathbf{f} = \rho_e(\mathbf{E} + \mathbf{v} \times \mathbf{B}) = \rho_e\mathbf{E} + \rho_e\mathbf{v} \times \mathbf{B} = \rho_e\mathbf{E} + \mathbf{J} \times \mathbf{B}, \tag{51}$$

where ρ_e is the charge density. Maxwell's first equation (the Gauss law for the electric field) reads

$$\nabla \cdot \mathbf{E} = \frac{\rho}{\varepsilon_0}, \tag{52}$$

where ε_0 is the vacuum electric permittivity. Maxwell's fourth equation (Ampere's circuital law with Maxwell's correction) reads

$$\nabla \times \mathbf{B} = \eta_0\mathbf{J} + \eta_0\varepsilon_0\frac{\partial\mathbf{E}}{\partial t}. \tag{53}$$

By substituting Eqs. (52) and (53) into Eq. (51), the Lorentz body force can be written as

$$\mathbf{f} = \varepsilon_0(\nabla \cdot \mathbf{E})\mathbf{E} + \frac{1}{\eta_0}(\nabla \times \mathbf{B}) \times \mathbf{B} - \varepsilon_0\frac{\partial\mathbf{E}}{\partial t} \times \mathbf{B}. \tag{54}$$

To solve the time derivative term of Eq. (54), Maxwell's third equation (Faraday's law of induction) and Maxwell's second equation (the Gauss law for magnetism) are introduced as

$$\nabla \times \mathbf{E} = -\frac{\partial\mathbf{B}}{\partial t}, \tag{55a}$$

$$\nabla \cdot \mathbf{B} = 0. \tag{55b}$$

By applying the above equations and the product rule, the following time derivative can be obtained:

$$\frac{\partial}{\partial t}(\mathbf{E} \times \mathbf{B}) = \frac{\partial\mathbf{E}}{\partial t} \times \mathbf{B} + \mathbf{E} \times \frac{\partial\mathbf{B}}{\partial t} = \frac{\partial\mathbf{E}}{\partial t} \times \mathbf{B} - \mathbf{E} \times (\nabla \times \mathbf{E}). \tag{56}$$

Then, the Lorentz body force can be further derived as

$$\begin{aligned} \mathbf{f} = & \varepsilon_0[(\nabla \cdot \mathbf{E})\mathbf{E} - \mathbf{E} \times (\nabla \times \mathbf{E})] + \frac{1}{\eta_0}[\mathbf{B}(\nabla \cdot \mathbf{B}) - \mathbf{B} \times (\nabla \times \mathbf{B})] \\ & - \varepsilon_0\frac{\partial}{\partial t}(\mathbf{E} \times \mathbf{B}). \end{aligned} \tag{57}$$

The magnetic dipole force for the non-conductive ferrofluid, i.e., the Kelvin magnetic force, which is derived from the Lorentz body force and the static Maxwell equation, can be presented as

$$\mathbf{F}_b^m = \frac{1}{\eta_0}[\mathbf{B}(\nabla \cdot \mathbf{B}) - \mathbf{B} \times (\nabla \times \mathbf{B})] = \mathbf{M}\nabla\mathbf{B} - \mathbf{M} \times \mathbf{J} = \mathbf{M}\nabla\mathbf{B}. \tag{58}$$

For the general Maxwell stress tensor, the following rule for eliminating the curls is introduced:

$$\frac{1}{2}\nabla(\mathbf{B} \cdot \mathbf{B}) = \mathbf{B} \times (\nabla \times \mathbf{B}) + (\mathbf{B} \cdot \nabla)\mathbf{B}. \tag{59}$$

Substituting the above equation into Eq. (57), the Lorentz body force can be further simplified as

$$\begin{aligned} \mathbf{f} = & \varepsilon_0\left[(\nabla \cdot \mathbf{E})\mathbf{E} - \frac{1}{2}\nabla(\mathbf{E} \cdot \mathbf{E}) + (\mathbf{E} \cdot \nabla)\mathbf{E}\right] + \frac{1}{\eta_0}[\mathbf{B}(\nabla \cdot \mathbf{B}) \\ & - \frac{1}{2}\nabla(\mathbf{B} \cdot \mathbf{B}) + (\mathbf{B} \cdot \nabla)\mathbf{B}] - \varepsilon_0\frac{\partial}{\partial t}(\mathbf{E} \times \mathbf{B}). \end{aligned} \tag{60}$$

Reorganizing the above equation, we can obtain the following equation:

$$\begin{aligned} \mathbf{f} = & \varepsilon_0[(\nabla \cdot \mathbf{E})\mathbf{E} + (\mathbf{E} \cdot \nabla)\mathbf{E}] + \frac{1}{\eta_0}[\mathbf{B}(\nabla \cdot \mathbf{B}) + (\mathbf{B} \cdot \nabla)\mathbf{B}] \\ & - \frac{1}{2}\nabla\left(\varepsilon_0E^2 + \frac{1}{\eta_0}B^2\right) - \varepsilon_0\frac{\partial}{\partial t}(\mathbf{E} \times \mathbf{B}). \end{aligned} \tag{61}$$

Thus, the total body force is given as

$$\mathbf{F} = \iiint_V \mathbf{f}dV = -\frac{d}{dt} \iiint_V \varepsilon_0(\mathbf{E} \times \mathbf{B})dV + \iiint_V \Pi dV, \tag{62a}$$

with

$$\begin{aligned} \Pi = & \varepsilon_0[(\nabla \cdot \mathbf{E})\mathbf{E} + (\mathbf{E} \cdot \nabla)\mathbf{E}] + \frac{1}{\eta_0}[\mathbf{B}(\nabla \cdot \mathbf{B}) + (\mathbf{B} \cdot \nabla)\mathbf{B}] \\ & - \frac{1}{2}\nabla\left(\varepsilon_0E^2 + \frac{1}{\eta_0}B^2\right). \end{aligned} \tag{62b}$$

By applying the divergence theorem, Eq. (62) can be transformed as⁴³

$$\mathbf{F} = -\frac{d}{dt} \iiint_V \varepsilon_0(\mathbf{E} \times \mathbf{B})dV + \iint_S \boldsymbol{\tau} \cdot \mathbf{n}dS, \tag{63a}$$

with

$$\begin{aligned} \tau_{ij} = & \varepsilon_0\left(E_iE_j - \frac{1}{2}\delta_{ij}E^2\right) + \frac{1}{\mu_0}\left(B_iB_j - \frac{1}{2}\delta_{ij}B^2\right) \\ = & \varepsilon_0\left(E_iE_j - \frac{1}{2}\delta_{ij}E^2\right) + \left(H_iB_j - \frac{\mu_0}{2}\delta_{ij}H^2\right). \end{aligned} \tag{63b}$$

Therefore, the magnetic stress tensor is given as

$$\tau_m = -\frac{\eta_0}{2} |\mathbf{H}|^2 \mathbf{I} + \mathbf{H}\mathbf{B}, \quad (64)$$

where \mathbf{I} denotes the identity operator. Then, the magnetic surface force can be derived as

$$\mathbf{F}_s^m = \nabla \cdot \tau_m = -\nabla \cdot \left(\frac{\mu_0}{2} |\mathbf{H}|^2 - \mathbf{H}\mathbf{B} \right). \quad (65)$$

To simplify the numerical model, the mathematical strategy of Rosensweig⁴³ is adopted. The magnetic body force is mathematically equivalent to the magnetic surface force, which becomes easy-to-implement and can be directly incorporated into the external force term of the LB model. Thus, the magnetic surface force term in Eq. (2) can be evaluated by

$$\mathbf{F}_m = \nabla \cdot \tau_m = -\frac{\mu_0}{2} \nabla (|\mathbf{H}|^2) + (\mathbf{B} \cdot \nabla) \mathbf{H} = -\frac{\mu_0 \chi}{2} \nabla |\mathbf{H}|^2. \quad (66)$$

F. Computational sequence

The computational sequence of the magnetic field coupling fractional-step-based LB model can be summarized as follows:

- (1) Initialize the fluid field and the magnetic field.
- (2) Specify the streaming distance δx . Determine the relaxation parameters τ_f and τ_g .
- (3) Evaluate the magnetic field through Eqs. (39a)–(39c).
- (4) Prediction step: use Eqs. (37a)–(37c) to evaluate the intermediate physical properties \tilde{p} , $\tilde{\rho}$, $\tilde{\mathbf{u}}$, and $\tilde{\mathbf{C}}$.
- (5) Implement the appropriate boundary conditions for the intermediate physical properties.
- (6) Correction step: use Eqs. (41a)–(41c) to update the macroscopic variables.
- (7) Implement the appropriate boundary conditions for the macroscopic variables, which are essentially the same as those imposed in step (5).
- (8) Repeat steps (3)–(7) until the computational convergence criterion is satisfied or the prescribed maximum iteration step is reached.

III. RESULTS AND DISCUSSION

In this section, several typical numerical tests are performed to validate the accuracy and capability of the proposed model. First, the grid independence study and the validation of the present method are examined by simulating a gas bubble rising in a stationary liquid and a stationary cylinder under a uniform magnetic field, respectively. Second, the magnetic field induced interfacial deformation of a ferrofluid droplet is simulated by the present numerical model and compared with the pioneering experimental result.⁴⁷ Third, to investigate the interfacial deformation of non-magnetic materials in magnetic multiphase flows, an aqueous droplet and a gas bubble in the ferrofluid under an external uniform magnetic field are simulated. Finally, a bubble rising in the ferrofluid under an external uniform magnetic field is investigated.

A. Grid independence study and validation

To ensure a grid independence solution and evaluate the accuracy of the present LB model, a grid sensitivity investigation is performed by simulating a gas bubble rising in a stationary liquid on different grid sizes with the same physical settings. In this case, the mass transfer and the complex interfacial behavior of the gas bubble are the consequences under the complicated interactions of surface tension force, gravitational effect (buoyancy force), inertial force, and viscous force. The characteristic length is set as the diameter of the bubble D . The key dimensionless parameters used in this simulation include the Reynolds number Re , the Eotvos number Eo , and the Froude number Fr , which are defined as $Re = \frac{\rho U D}{\mu}$, $Eo = \frac{\rho g D^2}{\sigma}$, and $Fr = \frac{U^2}{g D}$, respectively. The normalized time is given as $T = t \sqrt{\frac{g}{L}}$ with the iteration time t . For this grid independence test, a stationary gas bubble with the diameter $D = 0.5$ mm is located at a $2D \times 4D$ physical domain. Five different grid sizes of G1 (51×101), G2 (101×201), G3 (151×301), G4 (201×401), and G5 (251×501) are considered. The single bubble rises under the conditions of $Re = 40$, $Fr = 1$, the density ratio $\rho_L/\rho_G = 1000$, and the viscosity ratio $\mu_L/\mu_G = 100$. The interfacial thickness and the mobility are set to be 4 and 0.1, respectively. The no-slip boundary condition is employed on the top and bottom walls, and the periodic boundary condition is applied on the left and right walls.

Figures 1 and 2 show the time evolutions of the interfacial shape for the bubble rising at $Eo = 10$ and 50 under five different grid resolutions, respectively. The interfacial shapes at the same instantaneous time for different Eo are quite variform since Eo represents the ratio of the surface tension effect and gravitational effect. When a single gas bubble rises at a lower Eo of 10, a semicircular shape is formed although the surface tension force tends to restrain the gas bubble into a circular shape. When Eo increases to 50, a pair of tails appears at the edge of the gas bubble and develops during the rising process because the surface tension effect is reduced and cannot pull the stretched tails back to the main body. The differences in the interfacial shape can be hardly observed when the grid size is finer than G3, i.e., 151×301 .

Figure 3 compares the variation of the mass center with time for the bubble rising at $Eo = 10$ and 50, respectively. The mass center Y_p is defined as $Y_p = \frac{\int_{C < 0.5} y dx}{\int_{C < 0.5} 1 dx}$. Also included in Fig. 3 are the benchmark solutions of Wang *et al.*,⁴⁶ which are calculated by a mass-conserving multiphase LB flux solver based on a diffuse interface method. The mass center quantitatively represents the continuously rising motion of the bubble, and the differences in the trajectory of Y_p are negligible when the grid size is finer than G3. Figures 2 and 3 indicate that the present LB model can provide the grid independence solution if the grid size is fine enough. Moreover, the good agreement between the present results and those of Wang *et al.*⁴⁶ verifies the accuracy and the reliability of the present magnetic field coupling fractional-step-based LB model for the simulation of multiphase flows with a large density ratio and complex interfacial deformation.

To validate the accuracy and capability of the Poisson equation solver with a self-correcting procedure for the calculation of the external magnetic field, a stationary circular cylinder under an external uniform magnetic field is investigated. In this simulation, a two-dimensional circular cylinder with radius $R = 0.1$ mm is located at the center of a 1×1 mm² computational domain, which is

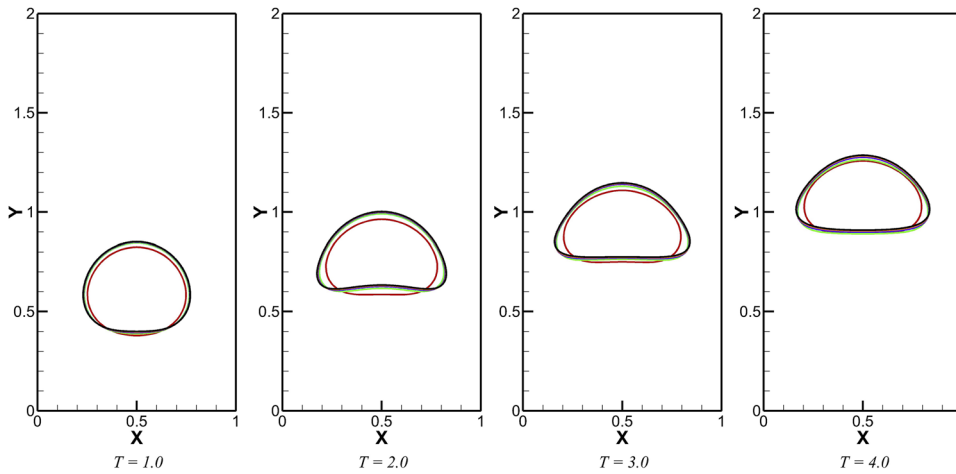


FIG. 1. Comparison of the interfacial shape for the bubble rising with $Eo = 10$ at the same instantaneous time under the grid sizes of G1 (red), G2 (green), G3 (purple), G4 (yellow), and G5 (black).

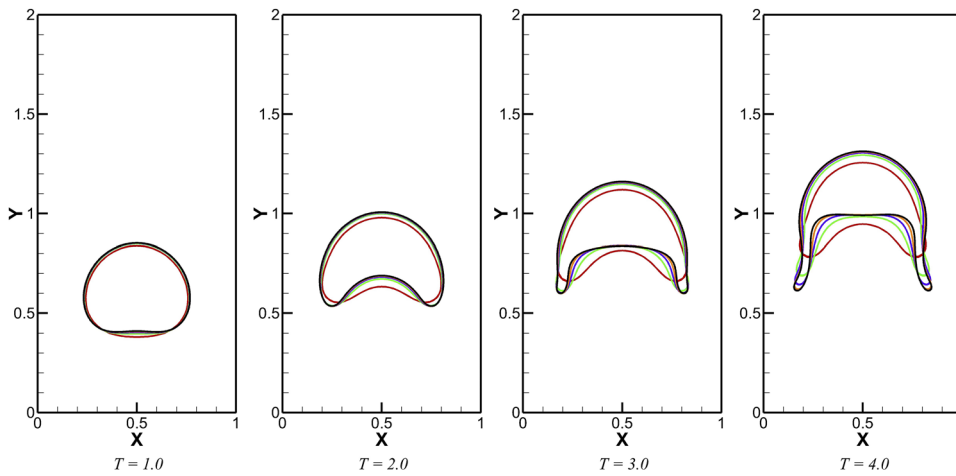


FIG. 2. Comparison of the interfacial shape for the bubble rising with $Eo = 50$ at the same instantaneous time under the grid sizes of G1 (red), G2 (green), G3 (purple), G4 (yellow), and G5 (black).

discretized by 201×201 lattice units. The initial magnetic field intensity H_0 is equal to 1.0 kA/m. The magnetic boundary condition on the top and bottom boundaries is

$$\frac{\partial \psi}{\partial y} = -H_0. \tag{67}$$

The magnetic insulation condition is imposed at the left and right boundaries as

$$\frac{\partial \psi}{\partial x} = 0. \tag{68}$$

The magnetic permeability of the circular cylinder is set as a fixed value, and thus, the magnetic field intensity around the circular cylinder solely depends on the magnetic permeability of the base fluid. Figure 4 compares the distribution of the magnetic flux density when η_1/η_2 is equal to 3 (magnetic cylinder) and 1/3 (non-magnetic cylinder). When the magnetic permeability of the stationary circular cylinder is larger than that of the base fluid, the magnetic circular is

easier to be magnetized than the surrounding based fluid, and thus, the streamlines around the magnetic cylinder tend to cross the interface, as shown in Fig. 4(a). On the contrary, the surrounding fluid is easier to be magnetized than the non-magnetic stationary circular cylinder when the magnetic permeability of the stationary circular cylinder is smaller than that of the base fluid, and thus, the streamlines around the magnetic cylinder avoid the interface, as shown in Fig. 4(b).

The magnetic field intensity inside the stationary circular cylinder under the external uniform magnetic field can be solved analytically, which is used as a benchmark solution to verify the present numerical result. The magnetic potential equation in Eq. (48) can be written in the polar coordinates as⁴³

$$\frac{\partial}{\partial r} \left(r \frac{\partial \psi}{\partial r} \right) + \frac{1}{r} \frac{\partial^2 \psi}{\partial \theta^2} = 0, \tag{69}$$

where r and θ are the radial and angular coordinates, respectively. By applying the method of separation of variable, the analytical

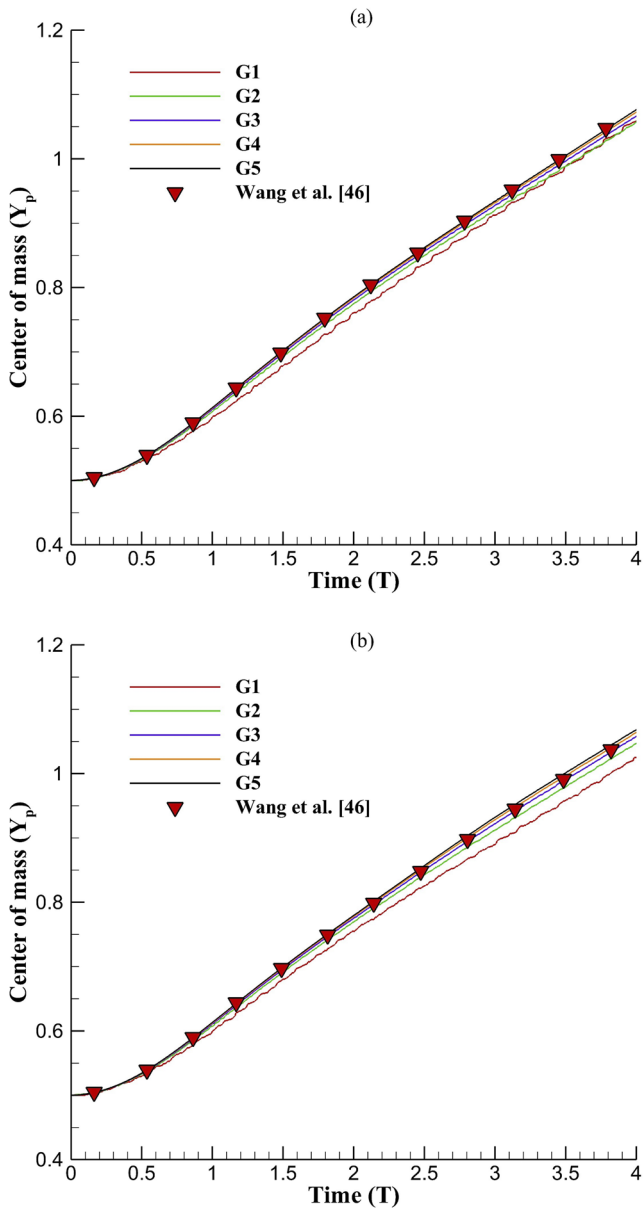


FIG. 3. Comparison of the mass center with the benchmark solutions for the bubble rising at (a) $Eo = 10$ and (b) $Eo = 50$.

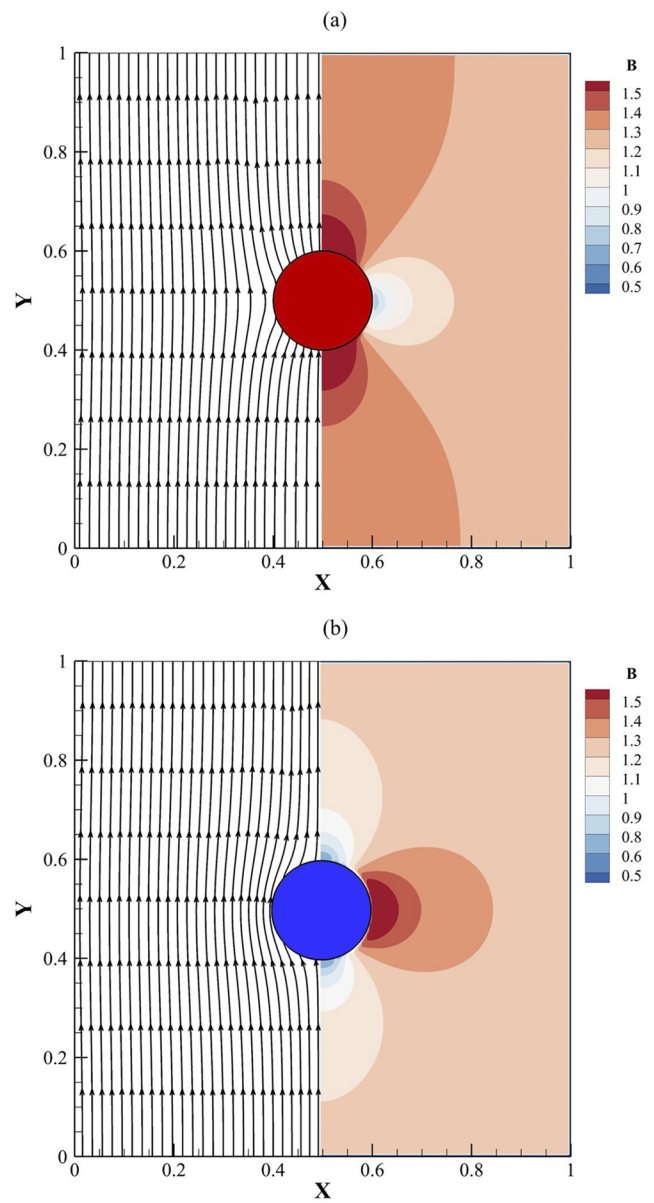


FIG. 4. The streamlines (left) and the contour (right) of magnetic flux density at different magnetic permeability ratios: (a) $\mu_1/\mu_2 = 3$ and (b) $\mu_1/\mu_2 = 1/3$.

solution of the magnetic field intensity inside the circular cylinder can be given as

$$\mathbf{H} = -\nabla\psi = \frac{2\mu_2}{\mu_1 + \mu_2}H_0 \sin\theta\mathbf{e}_r + \frac{2\mu_2}{\mu_1 + \mu_2}H_0 \cos\theta\mathbf{e}_\theta. \quad (70)$$

Figure 5 shows the variation of the magnetic intensity inside the stationary circular cylinder with the magnetic permeability ratio between the circular cylinder and the base fluid (η_1/η_2). A good agreement between the analytical and numerical results is observed,

which verifies the accuracy and capability of the Poisson equation solver with a self-correcting procedure for the calculation of the external magnetic field.

B. Magnetic field induced interfacial deformation of ferrofluid droplet

In this subsection, the interfacial deformation of a single water-based ferrofluid droplet immersed in organic oil under an external uniform magnetic field is simulated by using the present numerical

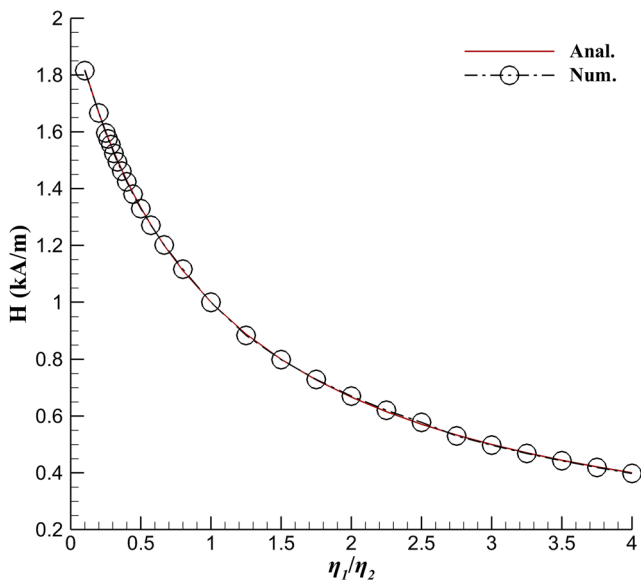


FIG. 5. The magnetic field intensity inside the stationary circular cylinder with a different magnetic permeability ratio between the circular cylinder and the base fluid.

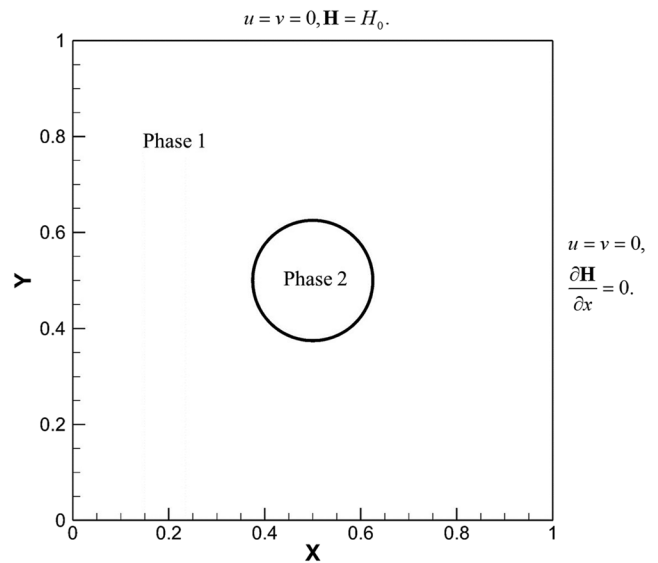


FIG. 6. The sketch of the geometric profiles and boundary conditions for the interfacial deformation of a single ferrofluid droplet under a uniform magnetic field.

method. Figure 6 shows the sketch of the geometric configuration and boundary conditions. Flament *et al.*⁴⁷ measured the deformation of a single ferrofluid droplet confined in a narrow gap between two parallel flat layers. Based on their experimental setup, this problem can be regarded as a two-dimensional multiphase flow under an external magnetic field. The interfacial deformation of the ferrofluid droplet showed a wide variety of equilibrium shapes under the uniform magnetic field, which is a consequence of the combinational effect of surface tension force, magnetic force, inertial force, and viscous force. Thus, the key dimensionless parameters involved in this simulation include the Reynolds number Re , the Weber number We , and the magnetic Bond number Bo_m , which are defined as $Re = \frac{\rho U D}{\mu}$, $We = \frac{\rho U^2 D}{\sigma}$, and $Bo_m = \frac{\eta H^2 D}{\sigma}$, respectively.

The physical parameters used in the numerical simulation are same as those in the experiment by Li *et al.*⁴⁵ The densities of ferrofluid and organic oil are 1580 kg/m^3 and 800 kg/m^3 , respectively. The density ratio and the viscosity ratio are set as 1.975 and 20, respectively. The surface tension coefficient and the relative magnetic susceptibility are 3.07 mN/m and 2.2, respectively. The computational domain is discretized by 201×201 lattice units, which has been found fine enough to generate the grid independent solution by our preliminary test. This interfacial deformation of a single ferrofluid droplet is simulated under the condition of $Re = 25.28$ and $We = 2.06$. The mobility and the interfacial thickness are set as 0.1 and 4, respectively. The no-slip boundary conditions are imposed at all the boundaries of the computational domain.

Figure 7 shows the interfacial deformations of a single ferrofluid droplet at the equilibrium stage for different $Bo_m = 0, 0.59, 2.36, 3.44, 5.60,$ and 12.38 . The red elliptical curves in Fig. 7 represent the interfacial position at the equilibrium stage obtained by

the present numerical model. Both the experimental and numerical results show that the interfacial deformations of a single ferrofluid droplet rely on the strength of the external magnetic field, and its elongations increase with Bo_m . To quantitatively investigate the elongation, the corresponding elongation ratio defined as the ratio between the semi-major axis a and the semi-minor axis b of the ferrofluid droplet in Fig. 7 is evaluated. The numerical result of the elongation ratio at the equilibrium stage obtained by the present model is plotted in Fig. 8, with the comparison of the experimental measurements by Flament *et al.*⁴⁷ and the computational results by Hu *et al.*³⁶ It can be seen that the present results agree well with the published data, which verifies the capability of the present numerical model to predict this magnetic multiphase flow. Compared with the experimental results, the difference at high Bo_m may be caused by the non-Newtonian effect of ferrofluid, which is non-negligible at a strong external magnetic field. However, the non-Newtonian effect of ferrofluid is the complicated combination of materials, the micro-structures of magnetic nanoparticles,⁹ the magnetization process,⁴⁵ etc., and the physical model is still lacking, which is, thus, not considered in this work.

To further investigate the dynamic deformation process of the single ferrofluid droplet, the time evolutions of the semi-major axis a and the semi-minor axis b of the ferrofluid droplet at different Bo_m are illustrated in Fig. 9. The interfacial shape of the ferrofluid droplet elongates immediately after the external magnetic field is applied and, then, experiences a damped oscillation period before reaching the equilibrium stage. In fact, this interfacial deformation process results from the competition between the magnetic force and the surface tension force. Generally, each magnetic nanoparticle dispersed in the base fluid becomes a tiny magnet under the magnetization of the external magnetic field, and thus, the entire ferrofluid droplet can be regarded as a magnetized magnet. The magnetic force

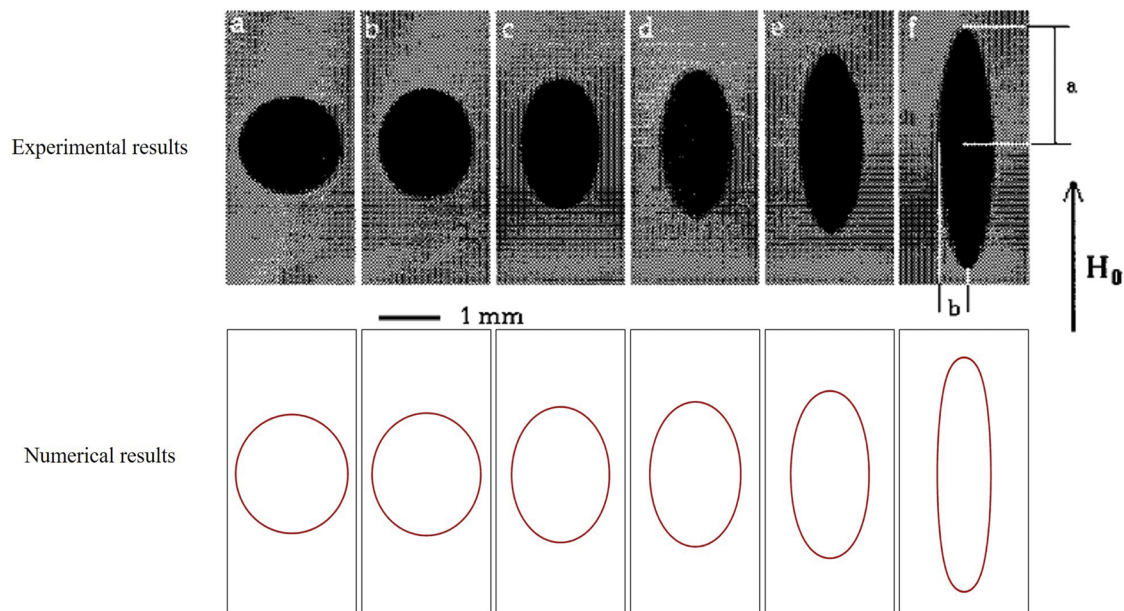


FIG. 7. The interfacial deformations of a single ferrofluid droplet at the equilibrium stage under different external uniform magnetic fields: (a) $Bo_m = 0$ ($H_0 = 0$ kA/m), (b) $Bo_m = 0.59$ ($H_0 = 1.2$ kA/m), (c) $Bo_m = 2.36$ ($H_0 = 2.4$ kA/m), (d) $Bo_m = 3.44$ ($H_0 = 2.9$ kA/m), (e) $Bo_m = 5.60$ ($H_0 = 3.7$ kA/m), and (f) $Bo_m = 12.38$ ($H_0 = 5.5$ kA/m) (top row: experiment results,⁴⁷ bottom row: numerical results). [Reproduced with permission from Flament *et al.*, “Measurements of ferrofluid surface tension in confined geometry,” *Phys. Rev. E* **53**(5), 4801–4806 (1996). Copyright 1996 American Physical Society].

tends to stretch the ferrofluid droplet into an elliptical shape along the external magnetic field direction; meanwhile, the surface tension force increases with curvature, which tends to restore its spherical shape.

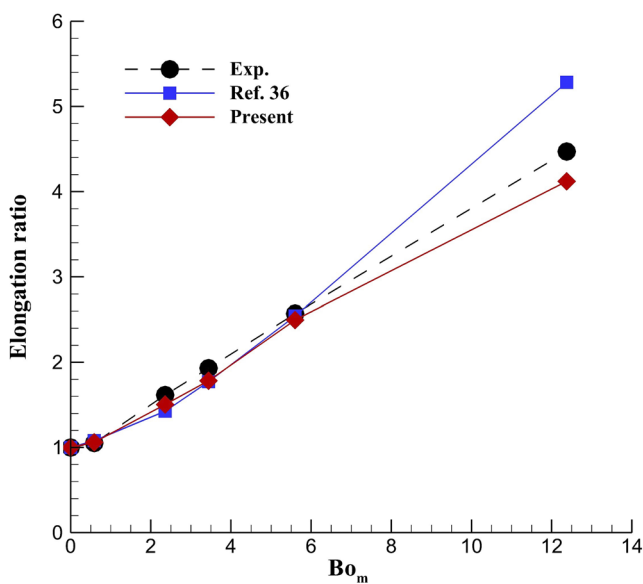


FIG. 8. The elongation ratio of a single ferrofluid droplet at the equilibrium stage with different external uniform magnetic fields.

The time evolutions of the elongation ratio of a single ferrofluid droplet at different Bo_m are presented in Fig. 10. It is found that both the amplitude and the oscillation period increase with Bo_m . Moreover, the elongation ratio of the ferrofluid droplet at the equilibrium stage is close to 1.0 when $Bo_m \leq 0.59$, which means that the interfacial shape is barely changed. In other words, the elongation caused by the magnetic force can be easily canceled by the surface tension force at a smaller Bo_m .

C. Interfacial deformation of non-magnetic material in ferrofluid

Controlling the interfacial shape of the non-magnetic droplet or bubble by the external magnetic field is nowadays one of the most popular areas of microfluidics. Recently, Rigoni *et al.*⁴⁸ experimentally investigated the interfacial behaviors of aqueous droplets in an oil-based ferrofluid under an external uniform magnetic field. Here, the present magnetic field coupling fractional-step-based LB model is used to simulate the same problem. The physical parameters used in the current numerical simulation are the same as those in the experiment.⁴⁸ The density ratio and the viscosity ratio are set as 2.0 and 20, respectively. The relative magnetic susceptibility is 1.4. The external magnetic field strengths are set to 0.608 kA/m, 1.2 kA/m, 1.8 kA/m, and 2.376 kA/m, which correspond to Bo_m of 0.43, 1.03, 1.63, and 2.47, respectively. The computational domain is discretized by 201×201 lattice units. This grid size is sufficiently small to produce the grid independent solution (data not shown). The mobility and the interfacial thickness are set as 0.6 and 4, respectively. The no-slip boundary condition is imposed at all the boundaries of the computational domain.

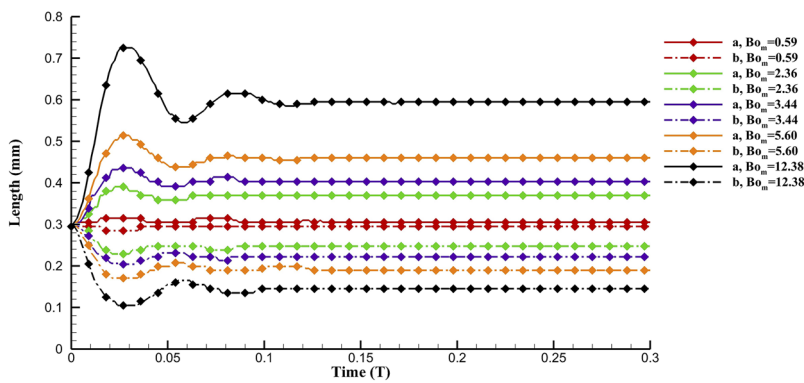


FIG. 9. The time evolutions of the semi-major axis a and the semi-minor axis b of the ferrofluid droplet at different Bo_m .

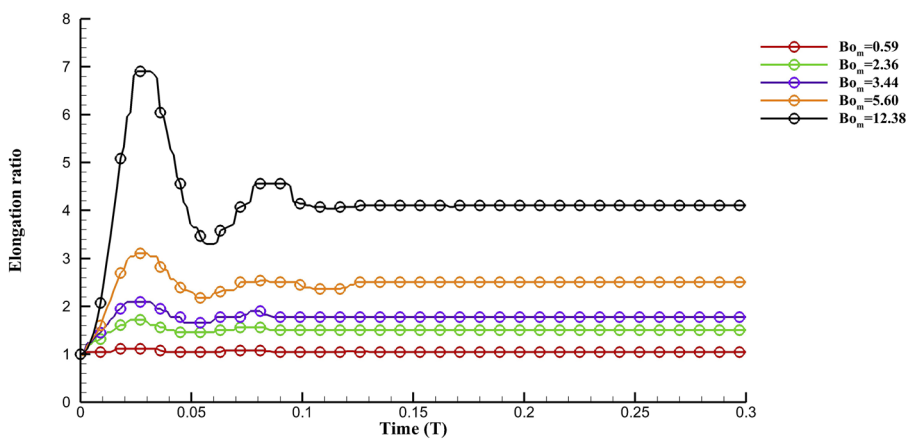


FIG. 10. The time evolutions of the elongation ratio for a single ferrofluid droplet at different Bo_m .

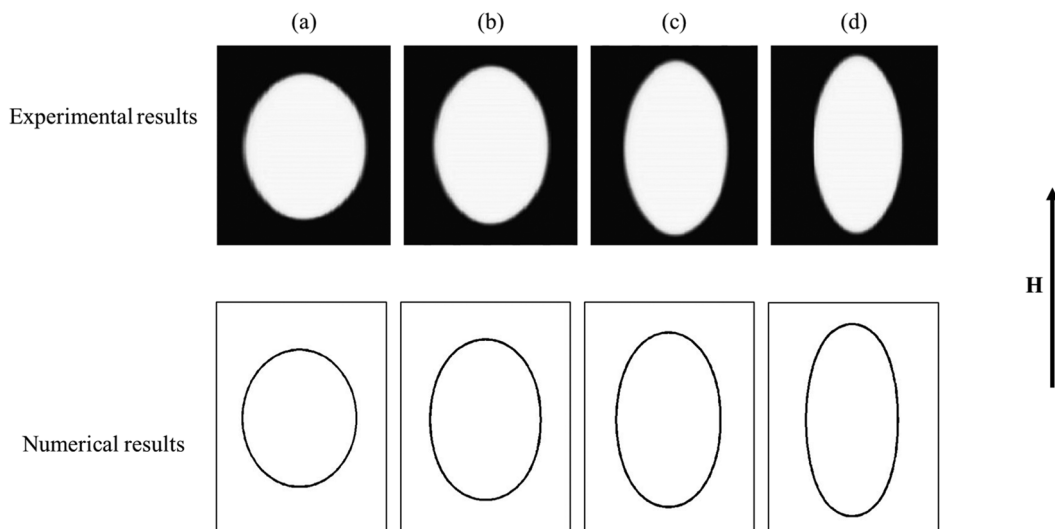


FIG. 11. The interfacial deformations of a single aqueous droplet in the ferrofluid at the equilibrium stage under different external uniform magnetic fields: (a) $Bo_m = 0.43$ ($H_0 = 0.608$ kA/m), (b) $Bo_m = 1.03$ ($H_0 = 1.2$ kA/m), (c) $Bo_m = 1.63$ ($H_0 = 1.8$ kA/m), and (d) $Bo_m = 2.47$ ($H_0 = 2.376$ kA/m) (top row: experiment results;⁴⁸ bottom row: numerical results). [Reproduced (adapted) with permission from Rigoni *et al.*, “Magnetic field-driven deformation, attraction, and coalescence of nonmagnetic aqueous droplets in an oil-based ferrofluid,” *Langmuir* **36**, 5048–5057 (2020). Copyright 2020 American Chemical Society].

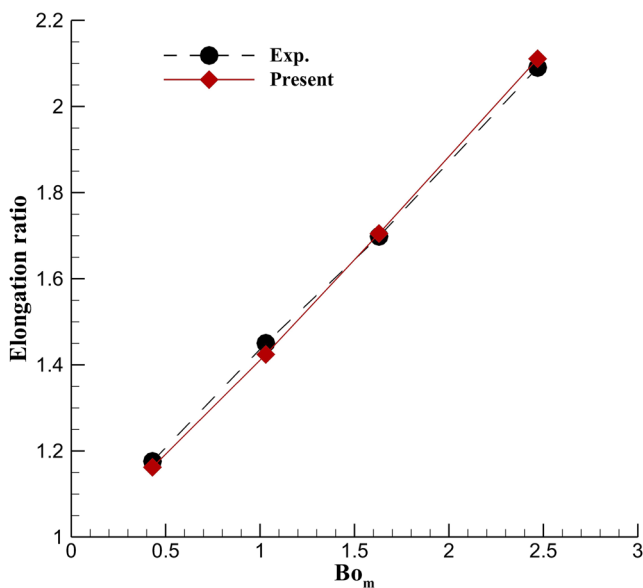


FIG. 12. Variation of the elongation ratio of a single aqueous droplet in the ferrofluid at the equilibrium stage with Bo_m .

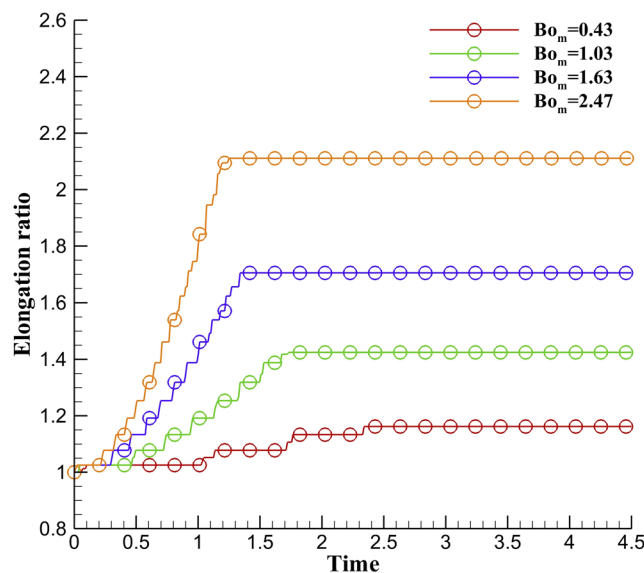


FIG. 13. The time evolutions of the elongation ratio for an aqueous droplet at different Bo_m .

The interfacial deformation of a single aqueous droplet in the ferrofluid at the equilibrium stage under different external uniform magnetic fields is shown in Fig. 11. The black elliptical curves represent the interfacial position at the equilibrium stage obtained by the present numerical model. To quantitatively investigate the elongation, the elongation ratio obtained by the present numerical model is plotted in Fig. 12 with the comparison of the experimental results.⁴⁸ The interfacial deformation of a single aqueous droplet shows the elliptical shape under an external uniform magnetic field, and its elongation ratio increases with Bo_m . The present numerical results show a good agreement with the experimental results.

Figure 13 shows the time evolutions of the elongation ratio for an aqueous droplet at $Bo_m = 0.43, 1.03, 1.63,$ and 2.47 . The elongation ratio of an aqueous droplet increases with Bo_m . Compared with Fig. 10, the time to reach the equilibrium stage for an aqueous droplet is longer than that of a ferrofluid droplet. Besides, the deformation process is relatively smooth, and the damped oscillation behavior does not appear because of the different deformation mechanisms caused by the different magnetization processes of the magnetic material and non-magnetic material shown in Fig. 4. The ferrofluid droplet can be magnetized, and thus, the interfacial deformation can be directly driven by the magnetic force inside the droplet. However, the magnetization of the non-magnetic aqueous droplet is very weak, and the magnetic force inside the droplet has a negligible effect on the interface. The streamlines of the magnetic flux density avoid passing through the interface of the aqueous droplet. Therefore, the magnetic flux density is stronger at the semi-minor axis of the aqueous droplet. After the magnetization process, the distribution of the magnetic flux density in the semi-minor axis of the non-magnetic aqueous droplet is similar to that in Fig. 4(b), and thus, the surrounding ferrofluid in the high magnetic flux density region is relatively strongly magnetized. The magnetic force

acted on the surrounding ferrofluid squeezes the aqueous droplet to deform into an elliptical shape. Therefore, the elongation ratio shown in Fig. 13 continuously increases with Bo_m .

To further investigate the effect of the external magnetic field on the non-magnetic fluids in magnetic multiphase flows with a large density ratio, the interfacial deformation of a gas bubble in the ferrofluid under an external uniform magnetic field is investigated

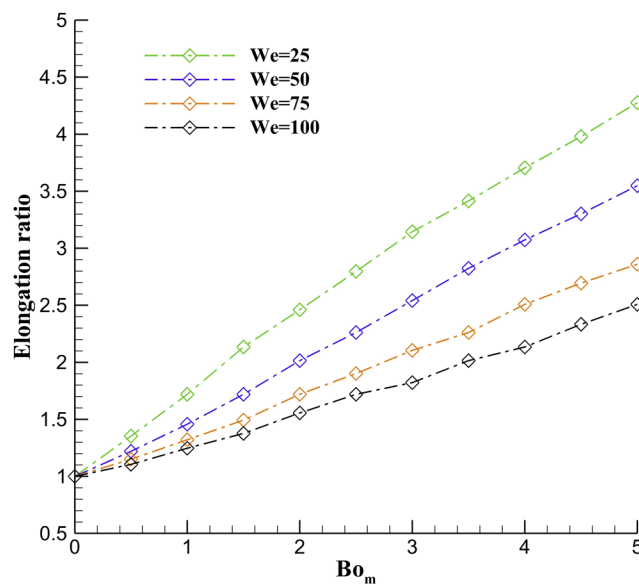


FIG. 14. The elongation ratio of a gas bubble in the ferrofluid at the equilibrium stage for different Bo_m and We .

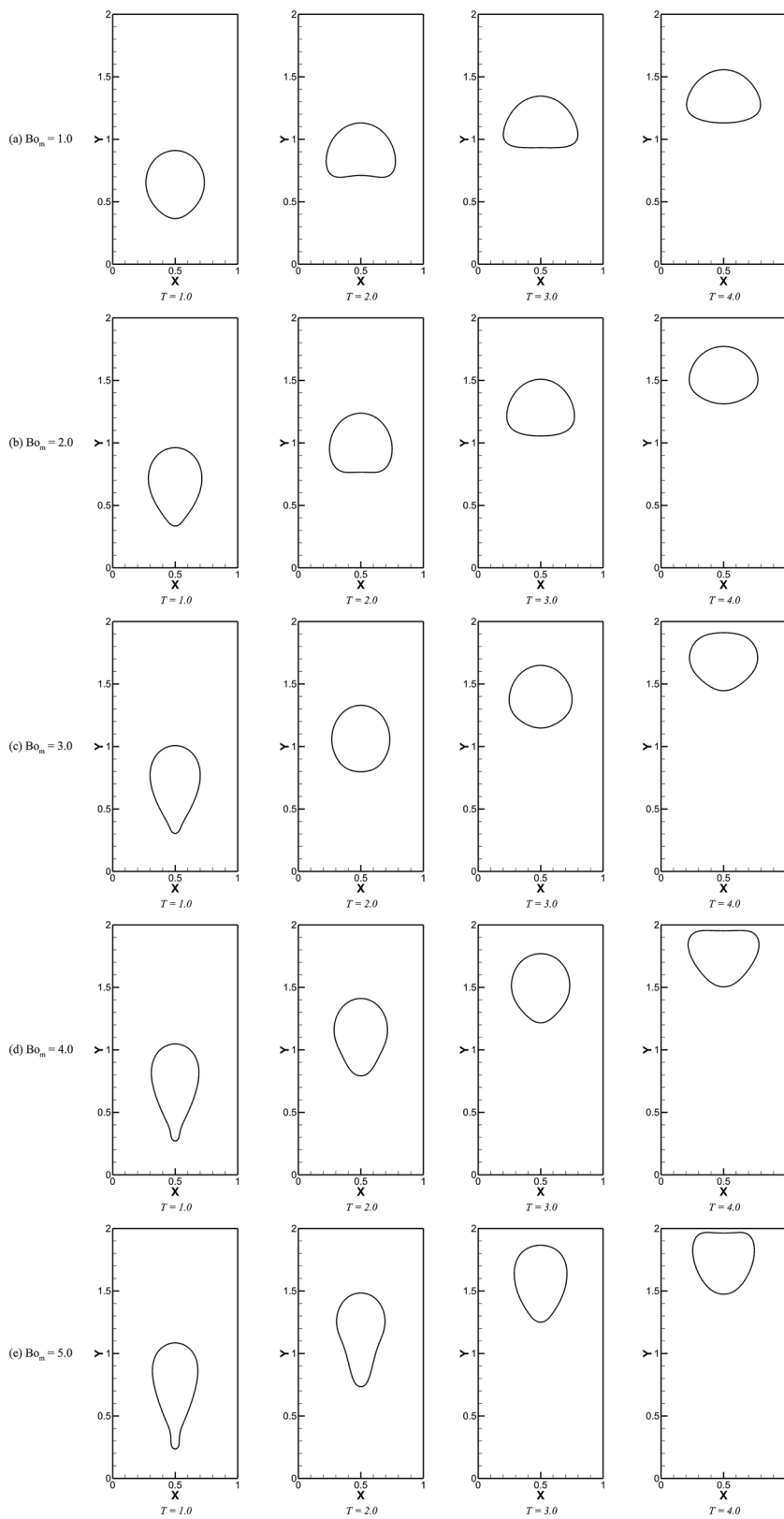


FIG. 15. The time evolutions of the interfacial shape for the bubble rising at $Eo = 10$ under different external uniform magnetic fields: (a) $Bo_m = 1.0$, (b) $Bo_m = 2.0$, (c) $Bo_m = 3.0$, (d) $Bo_m = 4.0$, and (e) $Bo_m = 5.0$.

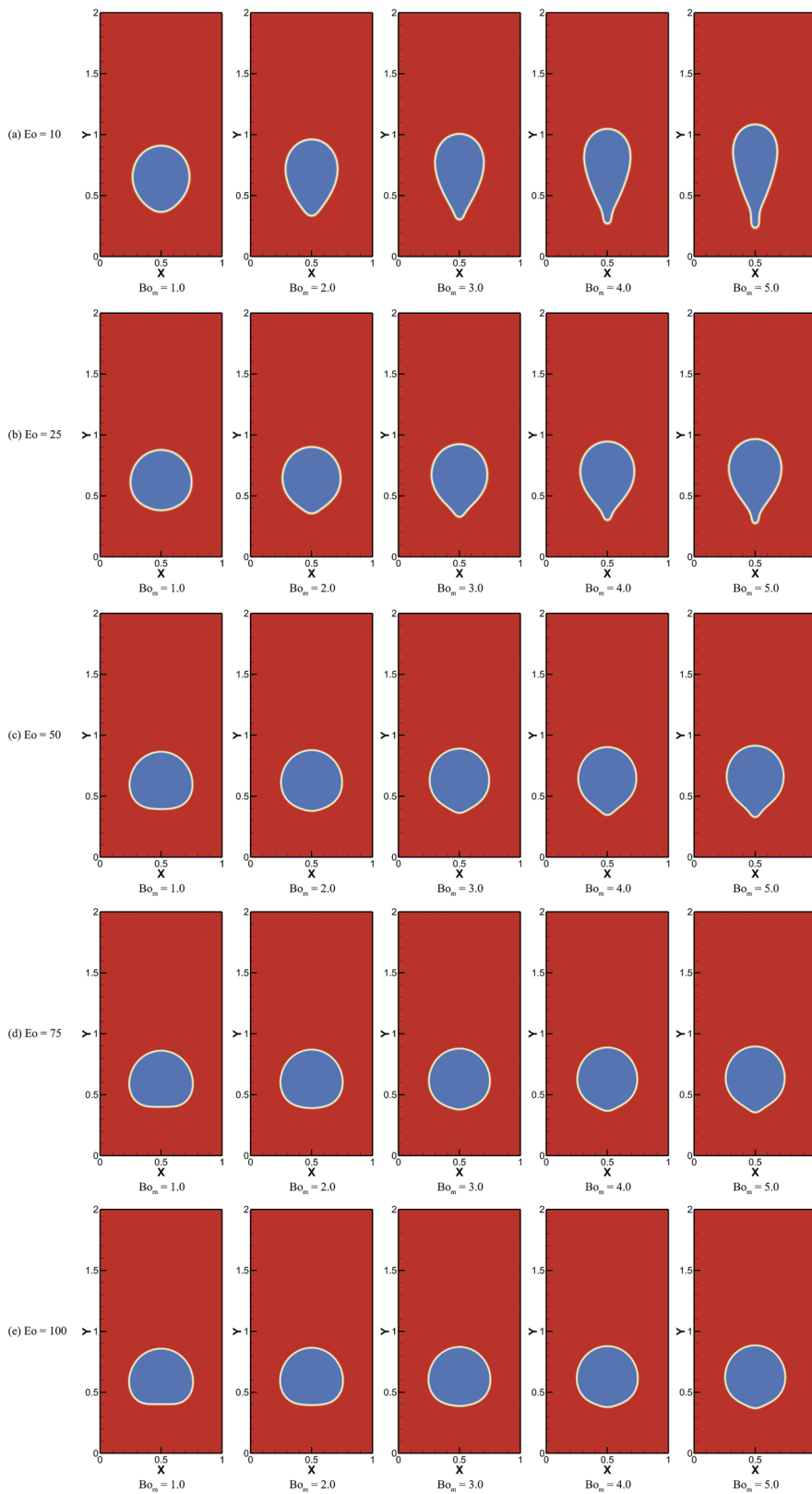


FIG. 16. The interfacial shape for the bubble rising at $T = 1.0$ under the external uniform magnetic field of Bo_m over the range of 1.0–5.0: (a) $Eo = 10$, (b) $Eo = 25$, (c) $Eo = 50$, (d) $Eo = 75$, and (e) $Eo = 100$.

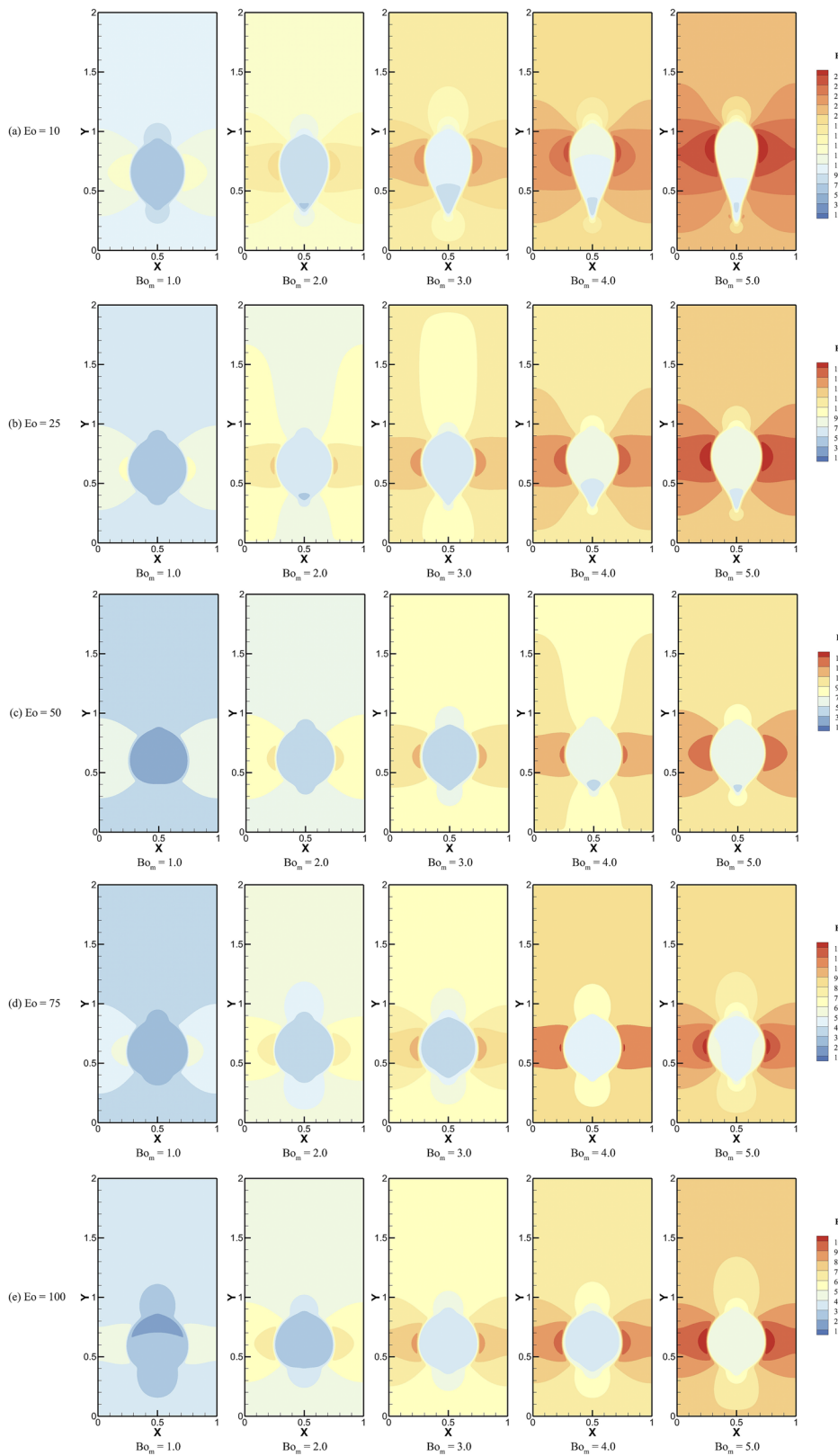


FIG. 17. The distribution of magnetic flux density for the bubble rising at $T = 1.0$ under the external uniform magnetic field of Bo_m over the range of 1.0–5.0: (a) $Eo = 10$, (b) $Eo = 25$, (c) $Eo = 50$, (d) $Eo = 75$, and (e) $Eo = 100$.

by the present numerical method. In the initial state, a gas bubble with the diameter $D = 0.5$ mm is located at the center of a $2D \times 3D$ computational domain, which is discretized by 201×301 lattice units. The density ratio and the viscosity ratio are set as 1000 and 100, respectively. The relative magnetic susceptibility is 2.2. This simulation is performed under the condition of $Re = 40$. The no-slip boundary condition is imposed at all the boundaries of the computational domain. Figure 14 shows the variation in the elongation ratio of a gas bubble in the ferrofluid at the equilibrium stage with Bo_m . The elongation ratio increases with an increase in Bo_m but decreases with an increase in We . As mentioned above, the elongation ratio depends on the strength of the external magnetic field. For a fixed Bo_m , a larger We represents a smaller surface tension coefficient of the gas bubble, which corresponds to a weaker magnetic field applied on the magnetic multiphase flow. For a fixed We , a larger Bo_m represents a stronger magnetic field, which is conducive to a larger elongation ratio.

D. Bubble rising in ferrofluid under an external magnetic field

The numerical simulations in Sec. III C neglect the effect of gravity and only focus on the interfacial deformation. However, in the real industrial applications, the mass transfer phenomenon of magnetic multiphase flows caused by the gravitational effect is quite important. In the following part, the mass transfer and the complex interfacial behavior of a gas bubble in the ferrofluid are simulated. The key dimensionless parameters involved in this simulation include the Reynolds number Re , the Eotvos number Eo , the magnetic Bond number Bo_m , and the Froude number Fr , which are defined as $Re = \frac{\rho UD}{\mu}$, $Eo = \frac{\rho g D^2}{\sigma}$, $Bo_m = \frac{\eta H^2 D}{\sigma}$, and $Fr = \frac{U^2}{gD}$, respectively. The normalized time is given as $T = t\sqrt{\frac{g}{L}}$ with the iteration time t . For this simulation, a gas bubble with the diameter $D = 0.5$ mm is located at a $2D \times 4D$ computational domain, which is discretized by 201×401 lattice units. Our preliminary study has demonstrated that this grid resolution is sufficiently fine to provide grid independent solution. The density ratio is 1000, and the viscosity ratio is 100. The bubble rising in the ferrofluid is simulated under the conditions of $Re = 40$ and $Fr = 1$. The magnetic field is in the opposite direction of gravity, and the relative magnetic susceptibility is 2.2. The interfacial thickness and the mobility are set to be 4 and 0.1, respectively. The no-slip boundary condition is employed on the top and bottom walls, and the periodic boundary condition is applied on the left and right walls.

Figure 15 shows the time evolutions of the interfacial shape for the bubble rising at $Eo = 10$ under different Bo_m . For a relatively weak magnetic field ($Bo_m = 1.0$), Fig. 15(a) shows that an elliptical shape appears at $T = 1.0$. The interfacial deformation and the rising process are similar to that in Fig. 1, but the rising velocity is accelerated by the external uniform magnetic field. When Bo_m is greater than 2.0, an inverted teardrop shape with a tail occurs at $T = 1.0$. The tail retracts back into the main body with the elapse of time due to the surface tension effect. With a further increase in Bo_m ($Bo_m > 3$), the length of the tail initially increases ($T = 1.0$), as shown in Figs. 15(b)–15(e). However, the tail does not retract but is trailed by the gas bubble ($T = 2.0$ and $T = 3.0$).

To investigate the inverted teardrop shape, Fig. 16 demonstrates the interfacial shape for the bubble rising at $T = 1.0$ under different Bo_m and Eo . It is clearly seen that the elongation ratio of the droplet and the length of tail initially increase ($T = 1.0$) with an increase in Bo_m but decrease with an increase in Eo . The main reason is that the surface tension force decreases with an increase in Eo , and the strength of the external magnetic force decreases with the surface tension force for a fixed Bo_m . The tail of the inverted teardrop shape shows a growing tendency with increasing Bo_m . When Eo is

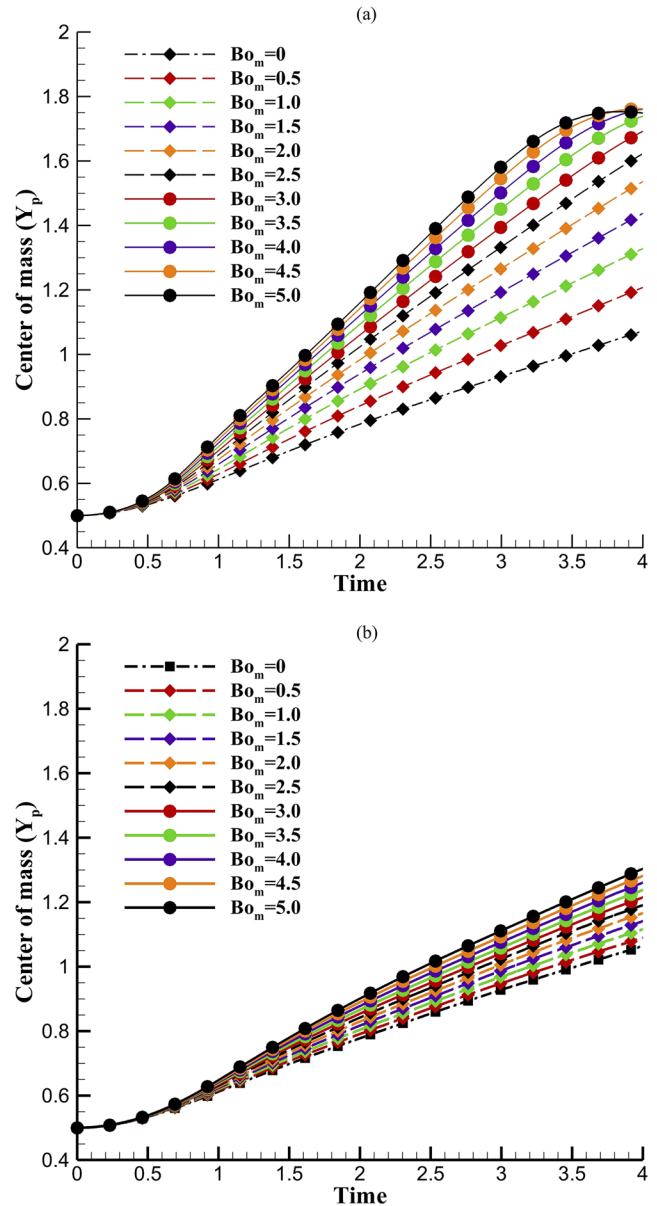


FIG. 18. The mass center for a single gas bubble rising in the ferrofluid under the different external uniform magnetic fields of Bo_m ranging from 0 to 5.0: (a) $Eo = 10$ and (b) $Eo = 50$.

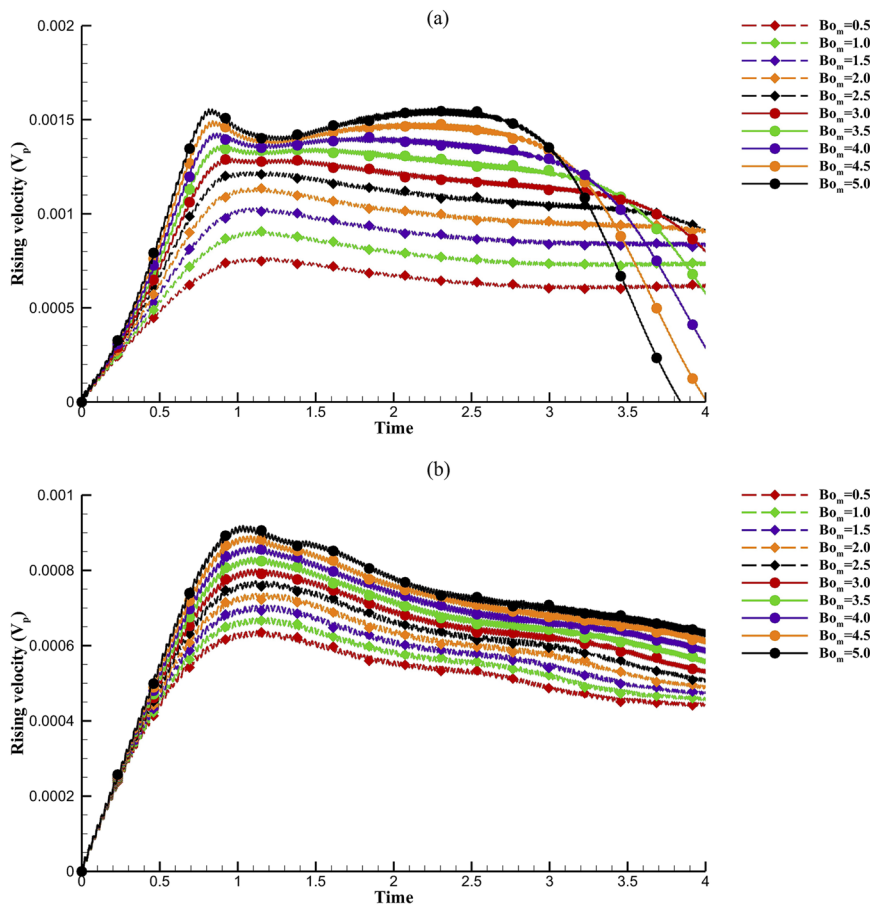


FIG. 19. The rising velocity for a single gas bubble rising in the ferrofluid under different Bo_m : (a) $Eo = 10$ and (b) $Eo = 50$.

less than 50, a clear inverted teardrop shape can be observed under a stronger external magnetic field ($Bo_m \geq 2.0$). The external magnetic field has a very small effect on the interfacial deformation of the gas bubble at $Eo = 50$ and with only a short tail trailing at the bottom of the gas bubble. When Eo further increases to 100, the strength of the external uniform magnetic field at a fixed Bo_m (within the range investigated in the present study) is too weak to drive the ferrofluid, and the interface of the gas bubble is barely affected by the external magnetic field.

The distribution of the magnetic flux density for the bubble rising at $T = 1.0$ under the external uniform magnetic field is presented in Fig. 17. A pair of higher magnetic flux density regions appears at the semi-minor axis of the gas bubble, which is the same as the distribution in Fig. 4(b) for the non-magnetic material. Therefore, the ferrofluid at these regions is magnetized with a relatively stronger magnetic force, which drives the gas bubble to deform into the elliptical shape. When $Eo \leq 50$, a lower magnetic flux density region can be clearly observed at the bottom of the gas bubble, where the surrounding ferrofluid cannot be well magnetized. Thus, the gas bubble close to this region is barely affected by the external uniform magnetic field. However, the gas bubble out of this region is accelerated by the magnetic force of the surrounding ferrofluid. Therefore, a tail is formed because the bottom of the gas bubble rises with a relatively

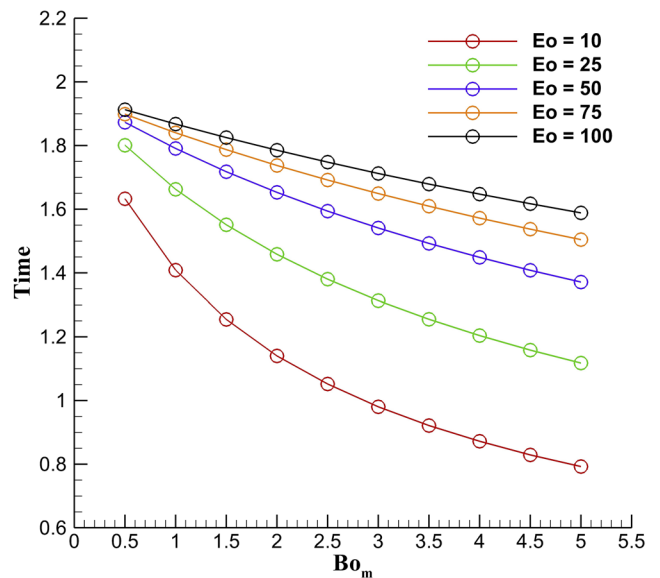


FIG. 20. The time when the head of the gas bubble reaches the center of the physical domain during the rising process under different Bo_m and Eo .

lower velocity. When $Eo > 50$, the lower magnetic flux density region almost spreads over the whole bubble, and thus, no tail is formed.

To quantitatively compare the effect of the external uniform magnetic field on the bubble rising process in the magnetic multiphase flow, the mass center (Y_p) for a single gas bubble rising in the ferrofluid with $Eo = 10$ and 50 under different Bo_m is recorded in Figs. 18(a) and 18(b), respectively. At the same instantaneous time, Y_p is higher at a larger Bo_m , which indicates that the bubble rising velocity increases with Bo_m . When $Eo = 10$ and $Bo_m \geq 4.0$, Y_p shows a decreasing tendency because the gas bubble reaches the top boundary of the computational domain. The comparison between Figs. 18(a) and 18(b) shows that Y_p is higher at a lower Eo , and the effect of Bo_m on Y_p is more pronounced at a lower Eo .

The time history of the velocity of the mass center V_p for $Eo = 10$ and 50 under different Bo_m is presented in Figs. 19(a) and 19(b), respectively. The velocity of the mass center is calculated by $V_p = \frac{\int_{C<0.5} v dx}{\int_{C<0.5} 1 dx}$. Figure 19(a) shows that at a lower Eo ($Eo = 10$), V_p shows an increasing tendency at the beginning and, then, tends to decrease until it reaches the plateau when $Bo_m \leq 2.5$. A decreasing tendency of the rising velocity in the end of the rising process

is observed when $Bo_m \geq 2.5$ because of the effect of top boundary of the computational domain. At a relatively higher Eo ($Eo = 50$), V_p first increases before it reaches the maximum velocity, and, then, shows a decreasing tendency. However, both the numerical results at $Eo = 10$ and 50 demonstrate that V_p can be accelerated by applying an external uniform magnetic field. The oscillation of the rising velocity can be observed in Fig. 19, and the oscillation amplitude increases with Bo_m . In fact, the mechanisms behind this kind of oscillation may be very complex, which include the inertial force effect, the resistance force effect, the magnetic force effect, the surface tension effect, etc. Figure 20 summarizes the time when the head of the gas bubble reaches the center of the physical domain during the rising process under different Bo_m , which decreases with an increase in Bo_m .

The magnetic energy of the external magnetic field is defined as $E_{mag} = \frac{1}{2} \mu |H|^2$. The time evolutions of the magnetic energy at the center point of the computational domain ($[X, Y] = [0.5, 1.0]$) during the rising process at $Eo = 10$ and 50 are calculated and plotted in Figs. 21(a) and 21(b), respectively. There are three valleys of magnetic energy in Fig. 21(a): (1) the first valley appears at the

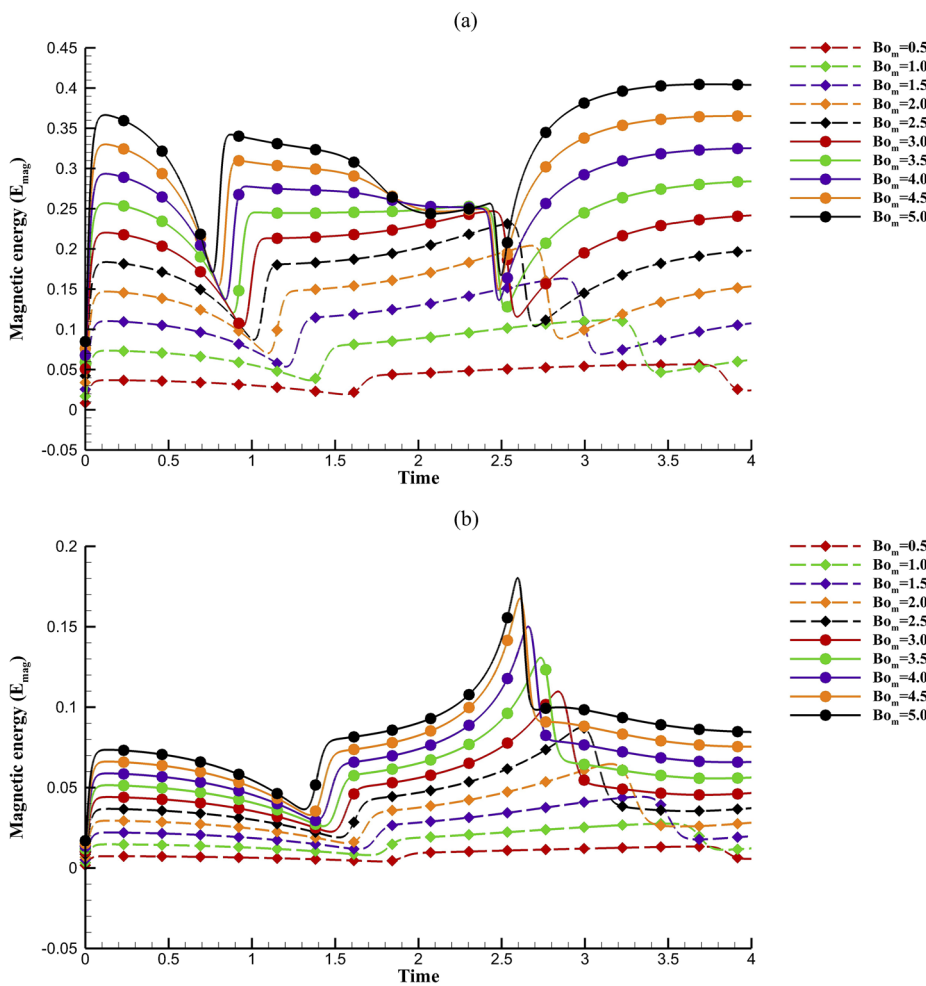


FIG. 21. The time evolutions of magnetic energy at the center of the physical domain during the rising process under different Bo_m : (a) $Eo = 10$ and (b) $Eo = 50$.

initial time, which represents the magnetization process; (2) the second valley shows that the head of the gas bubble approaches the monitoring point, which corresponds to the relatively lower magnetic flux density region on the head of the gas bubble; and (3) the third valley shows that the gas bubble leaves the monitoring point, which corresponds the lower magnetic flux density region on the bottom of the gas bubble. When $Bo_m \geq 4.0$, a small valley appears before the third valley in Fig. 21(a), which represents the low magnetic flux density region inside the tail of the gas bubble because the inverted teardrop shape is fully developed under the effect of the strong external magnetic field. Compared with Fig. 21(a), Fig. 21(b) shows that each magnetic energy curve at $E_0 = 50$ also has three similar valleys, but the magnetic energy rapidly increases before reaching the third valley.

IV. CONCLUSION

Magnetic multiphase flows widely occur in microfluidics, drug delivery, and heat transfer. The present work introduces a magnetic field coupling fractional-step-based multiphase LB model to simulate incompressible magnetic multiphase flows, which offers the following advantages: (1) the proposed numerical model inherits the excellent performance of kinetic theory from the LB method and integrates the good numerical stability from the fractional-step method; (2) the evolution of the distribution function does not need to be solved, which efficiently saves the virtual memories efficiently; (3) the magnetic field with the magnetic flux density interaction between the magnetic and non-magnetic regions is evaluated by the Poisson equation solver with a self-correcting procedure; (4) through the rigorous mathematical procedure, the magnetic force becomes easy-to-implement and can be directly incorporated into the external force term.

The grid independence study is first investigated by simulating a gas bubble rising in a stationary liquid. The mass center of the gas bubble during the rising process under the fine grid size (151×301) shows a good agreement with the benchmark results.⁴⁴ The validation for the magnetic field solver is, then, examined by computing a stationary cylinder under a uniform magnetic field, and the result agrees well with the analytical solution of the static magnetic Maxwell equation obtained by the separation of variables method. After that, the interfacial deformations of a ferrofluid droplet in organic oil and an aqueous droplet in the ferrofluid are simulated. Although the interfacial deformations are similar for the two cases, the underlying mechanisms are different. For the ferrofluid droplet, the magnetic nanoparticles dispersed in it are magnetized, and it is, then, stretched by the magnetic force inside the droplet. However, for the aqueous droplet, the magnetic flux density on the semi-minor axis of the droplet is larger, and the surrounding ferrofluid is strongly magnetized, which squeezes the aqueous droplet into an elliptical shape. Furthermore, the elongation ratios of the ferrofluid droplet, the aqueous droplet, and the gas bubble are investigated, which increase with Bo_m . Finally, a single gas bubble rising in the ferrofluid under the external uniform magnetic field is investigated, which shows that the effect of the external magnetic field in the opposite direction of gravity can accelerate the rising process. All the simulation cases demonstrate the capability and potential of the present method for simulating complex fluid dynamics problems

associated with the interfacial deformation in magnetic multiphase flows.

ACKNOWLEDGMENTS

This work was supported by the Department of Education of Guangdong Province (Grant No. 2020KZDZX1185), the Shenzhen Key Laboratory of Complex Aerospace Flows (Grant No. ZDSYS201802081843517), the Guangdong Provincial Key Laboratory of Turbulence Research and Applications (Grant No. 2019B21203001), and the National Natural Science Foundation of China (NSFC, Grant Nos. 91852205, 91741101, and 11961131006). X. Li and Z. Q. Dong would like to thank the Postgraduate Innovation Funds of Southern University of Science and Technology (Grant No. Y01301803) for the financial support. Numerical simulations in this work are supported by the Center for Computational Science and Engineering at the Southern University of Science and Technology.

DATA AVAILABILITY

The data that support the findings of this study are available from the corresponding author upon reasonable request.

REFERENCES

- 1 F. Bitter, "On inhomogeneities in the magnetization of ferromagnetic materials," *Phys. Rev.* **38**(10), 1903 (1931).
- 2 W. C. Elmore, "Ferromagnetic colloid for studying magnetic structures," *Phys. Rev.* **54**(4), 309 (1938).
- 3 W. C. Elmore, "The magnetization of ferromagnetic colloids," *Phys. Rev.* **54**(12), 1092 (1938).
- 4 J. L. Neuringer and R. E. Rosensweig, "Ferrohydrodynamics," *Phys. Fluids* **7**, 1927 (1964).
- 5 M. D. Cowley and R. E. Rosensweig, "The interfacial stability of a ferromagnetic fluid," *J. Fluid Mech.* **30**, 671 (1967).
- 6 A. B. Guimarães, F. R. Cunha, and R. G. Gontijo, "The influence of hydrodynamic effects on the complex susceptibility response of magnetic fluids undergoing oscillatory fields: New insights for magnetic hyperthermia," *Phys. Fluids* **32**, 012008 (2020).
- 7 H. Massana-Cid, F. Meng, D. Matsunaga, R. Golestanian, and P. Tierno, "Tunable self-healing of magnetically propelling colloidal carpets," *Nat. Commun.* **10**, 2444 (2019).
- 8 C. Kumar, M. Hejazian, C. From, S. C. Saha, E. Sauret, Y. Gu, and N.-T. Nguyen, "Modeling of mass transfer enhancement in a magnetofluidic micromixer," *Phys. Fluids* **31**(6), 063603 (2019).
- 9 X. Li, P. Yu, X. Niu, H. Yamaguchi, and D. Li, "Non-contact manipulation of nonmagnetic materials by using a uniform magnetic field: Experiment and simulation," *J. Magn. Magn. Mater.* **497**, 165957 (2020).
- 10 T. Hayat, M. I. Khan, M. Imtiaz, A. Alsaedi, and M. Waqas, "Similarity transformation approach for ferromagnetic mixed convection flow in the presence of chemically reactive magnetic dipole," *Phys. Fluids* **28**, 102003 (2016).
- 11 H. Yamaguchi and T. Bessho, "Long distance heat transport device using temperature sensitive magnetic fluid," *J. Magn. Magn. Mater.* **499**, 166248 (2020).
- 12 Lord Rayleigh, "XX. On the theory of surface forces. II. Compressible fluids," *Philos. Mag.* **33**, 209 (1892).
- 13 J. D. van der Waals, "Thermodynamische theorie der kapillarität unter voraussetzung stetiger dichteänderung," *Z. Phys. Chem.* **13**, 657 (1894); "The thermodynamic theory of capillarity under the hypothesis of a continuous variation of density," *J. Stat. Phys.* **20**, 200 (1979) (in English).

- ¹⁴G. I. Taylor, "The formation of emulsions in definable fields of flow," *Proc. R. Soc. A* **146**, 501–523 (1934).
- ¹⁵D. M. Anderson, G. B. McFadden, and A. A. Wheeler, "Diffuse-interface methods in fluid mechanics," *Annu. Rev. Fluid Mech.* **30**, 139 (1998).
- ¹⁶S. Chen and G. D. Doolen, "Lattice Boltzmann method for fluid flows," *Annu. Rev. Fluid Mech.* **30**, 329–364 (1998).
- ¹⁷C. K. Aidun and J. R. Clausen, "Lattice-Boltzmann method for complex flows," *Annu. Rev. Fluid Mech.* **42**, 439–472 (2010).
- ¹⁸T. W. Zhang, J. Wu, and X. J. Lin, "Numerical investigation on formation and motion of bubble or droplet in quiescent flow," *Phys. Fluids* **32**, 032106 (2020).
- ¹⁹X. Shan and H. Chen, "Lattice Boltzmann model for simulating flows with multiple phases and components," *Phys. Rev. E* **47**(3), 1815–1819 (1993).
- ²⁰X. He, S. Chen, and R. Zhang, "A lattice Boltzmann scheme for incompressible multiphase flow and its application in simulation of Rayleigh–Taylor instability," *J. Comput. Phys.* **152**, 642–663 (1999).
- ²¹H. W. Zheng, C. Shu, and Y. T. Chew, "A lattice Boltzmann model for multiphase flows with large density ratio," *J. Comput. Phys.* **218**, 353–371 (2006).
- ²²H. Huang, J.-J. Huang, and X.-Y. Lu, "A mass-conserving axisymmetric multiphase lattice Boltzmann method and its application in simulation of bubble rising," *J. Comput. Phys.* **269**, 386–402 (2014).
- ²³Y. Wang, C. Shu, H. B. Huang, and C. J. Teo, "Multiphase lattice Boltzmann flux solver for incompressible multiphase flows with large density ratio," *J. Comput. Phys.* **280**, 404–423 (2015).
- ²⁴X.-D. Niu, Y. Li, Y.-R. Ma, M.-F. Chen, X. Li, and Q.-Z. Li, "A mass-conserving multiphase lattice Boltzmann model for simulation of multiphase flows," *Phys. Fluids* **30**(1), 013302 (2018).
- ²⁵H. Z. Yuan, Y. Wang, and C. Shu, "An adaptive mesh refinement-multiphase lattice Boltzmann flux solver for simulation of complex binary fluid flows," *Phys. Fluids* **29**, 123604 (2017).
- ²⁶Z. Chen, C. Shu, Y. Wang, L. M. Yang, and D. Tan, "A simplified lattice Boltzmann method without evolution of distribution function," *Adv. Appl. Math. Mech.* **9**(1), 1–22 (2017).
- ²⁷Z. Chen, C. Shu, and D. Tan, "A truly second-order and unconditionally stable thermal lattice Boltzmann method," *Appl. Sci.* **7**(3), 277 (2017).
- ²⁸Z. Chen, C. Shu, and D. Tan, "High-order simplified thermal lattice Boltzmann method for incompressible thermal flows," *Int. J. Heat Mass Transfer* **127**, 1–16 (2018).
- ²⁹Z. Chen, C. Shu, D. Tan, X. D. Niu, and Q. Z. Li, "Simplified multiphase lattice Boltzmann method for simulating multiphase flows with large density ratios and complex interfaces," *Phys. Rev. E* **98**, 063314 (2018).
- ³⁰Z. Chen, C. Shu, L. Yang, X. Zhao, and N. Liu, "Immersed boundary–simplified thermal lattice Boltzmann method for incompressible thermal flows," *Phys. Fluids* **32**, 013605 (2020).
- ³¹X. D. Niu, H. Yamaguchi, and K. Yoshikawa, "Lattice Boltzmann model for simulating temperature-sensitive ferrofluids," *Phys. Rev. E* **79**, 046713 (2009).
- ³²T. Zhang and D. Che, "Double MRT thermal lattice Boltzmann simulation for MHD natural convection of nanofluids in an inclined cavity with four square heat sources," *Int. J. Heat Mass Transfer* **94**, 87–100 (2016).
- ³³H. Sajjadi, A. A. Delouei, M. Atashafrooz, and M. Sheikholeslami, "Double MRT lattice Boltzmann simulation of 3-D MHD natural convection in a cubic cavity with sinusoidal temperature distribution utilizing nanofluid," *Int. J. Heat Mass Transfer* **126**, 489–503 (2018).
- ³⁴D. Shi, Q. Bi, and R. Zhou, "Numerical simulation of a falling ferrofluid droplet in a uniform magnetic field by the VOSET method," *Numer. Heat Transfer, Part A* **66**(2), 144–164 (2014).
- ³⁵A. Ghaderi, M. H. Kayhani, and M. Nazari, "Numerical investigation on falling ferrofluid droplet under uniform magnetic field," *Eur. J. Mech.: B/Fluids* **72**, 1–11 (2018).
- ³⁶Y. Hu, D. C. Li, and X. D. Niu, "Phase-field-based lattice Boltzmann model for multiphase ferrofluid flows," *Phys. Rev. E* **98**, 033301 (2018).
- ³⁷J. Kim and P. Moin, "Application of a fractional-step method to incompressible Navier–Stokes equations," *J. Comput. Phys.* **59**, 308–323 (1985).
- ³⁸H. Araseki and S. Kotake, "A self-correcting procedure for computational liquid metal magnetohydrodynamics," *J. Comput. Phys.* **110**, 301–309 (1994).
- ³⁹J. W. Cahn and J. E. Hilliard, "Free energy of a nonuniform system. I. Interfacial free energy," *J. Chem. Phys.* **28**(2), 258–267 (1958).
- ⁴⁰D. Jacqmin, "Contact-line dynamics of a diffuse fluid interface," *J. Fluid Mech.* **402**, 57–88 (2000).
- ⁴¹Y. H. Qian, D. D’Humières, and P. Lallemand, "Lattice BGK models for Navier–Stokes equation," *Europhys. Lett.* **17**(6), 479–484 (1992).
- ⁴²S. Chapman and T. G. Cowling, *The Mathematical Theory of Non-Uniform Gases* (Cambridge University Press, Cambridge, 1970).
- ⁴³R. E. Rosensweig, *Ferrohydrodynamics* (Cambridge University Press, Cambridge, 1985).
- ⁴⁴M. F. Chen, X. Li, X. D. Niu, Y. Li, A. Khan, and H. Yamaguchi, "Sedimentation of two non-magnetic particles in magnetic fluid," *Acta Phys. Sin.* **66**, 164703 (2017).
- ⁴⁵X. Li, X.-D. Niu, Y. Li, and M.-F. Chen, "Self-assembly of silica microparticles in magnetic multiphase flows: Experiment and simulation," *Phys. Fluids* **30**, 040905 (2018).
- ⁴⁶Y. Wang, C. Shu, J. Y. Shao, J. Wu, and X. D. Niu, "A mass-conserved diffuse interface method and its application for incompressible multiphase flows with large density ratio," *J. Comput. Phys.* **290**, 336–351 (2015).
- ⁴⁷C. Flament, S. Laci, J.-C. Bacri, A. Cebers, S. Neveu, and R. Perzynski, "Measurements of ferrofluid surface tension in confined geometry," *Phys. Rev. E* **53**(5), 4801–4806 (1996).
- ⁴⁸C. Rigoni, J. Fresnais, D. Talbot, R. Massart, R. Perzynski, J.-C. Bacri, and A. Abou-Hassan, "Magnetic field-driven deformation, attraction, and coalescence of nonmagnetic aqueous droplets in an oil-based ferrofluid," *Langmuir* **36**, 5048–5057 (2020).